

# Longitudinal Control Law Design and Handling Qualities Optimization for a Business Jet Flight Control System

Tom Berger\*

*University Affiliated Research Center, Moffett Field, CA*

Mark B. Tischler†

*U.S. Army Aeroflightdynamics Directorate, Moffett Field, CA*

Steven G. Hagerott‡

*Cessna Aircraft Company, Wichita, KS*

Dagfinn Gangsaas§

Nomaan Saeed¶

*Aerospace Control Dynamics LLC, Minden, NV*

A comprehensive set of stability, handling qualities, and performance specifications was used to drive the optimization of commonly used fixed-wing longitudinal control laws applied to a business jet. The specifications were divided into two tiers. The first were the key flight control and handling qualities requirements and were used directly for optimization, while the second were used as a check afterwards. Similarities between the commonly used longitudinal control laws investigated in this study and a model following controller were exploited to explicitly set feed-forward gains to provide good handling qualities. A linear-quadratic regulator method was employed for preliminary design as a way to initialize the control law feedback gain values for optimization. A multi-objective parametric optimization approach was then used to arrive at feedback gains that concurrently satisfy all specifications. Using this optimization approach, the trade-offs of increased crossover frequency were investigated. In addition, a smooth gain schedule was generated by optimizing the control law parameters of different flight conditions to meet the same requirements. This paper describes the control law architecture used as well as the optimization approach, the specifications used, and the design results.

## Nomenclature

$\alpha$	Angle-of-attack [deg, rad]
$\alpha_{cmd}$	Angle-of-attack command [rad]
$\alpha_{nz}$	Steady state angle-of-attack per normal load factor [rad/g]
$\bar{q}$	Dynamic pressure [psf]
$\delta_{act}$	Actuator position [deg]
$\delta_{stk}$	Stick force [lb]
$\dot{\alpha}$	Angle-of-attack rate [deg/sec, rad/sec]
$\dot{\alpha}_{cmd}$	Angle-of-attack rate command [rad/sec]
$\dot{\delta}_{act}$	Actuator rate [deg/sec]

\*Research Engineer, University Affiliated Research Center, Senior Member AIAA.

†Flight Control Technology Group Leader, Senior Scientist, U.S. Army Aeroflightdynamics Directorate, Associate Fellow AIAA.

‡Engineer Specialist, Cessna Aircraft Company, Senior Member AIAA.

§President, Aerospace Control Dynamics LLC., Associate Fellow AIAA.

¶Chief Engineer/VP, Aerospace Control Dynamics LLC., Member AIAA.

This material is declared a work of the U.S. Government and is not subject to copyright protection in the United States.

$\dot{n}_{zcmd}$	Commanded normal load factor rate [g/sec]
$\dot{q}$	Pitch acceleration [rad/sec <sup>2</sup> ]
$\omega_c$	Crossover frequency [rad/sec]
$\omega_n$	Natural frequency [rad/sec]
$\omega_\alpha$	LQR output shaping function frequency of complex-pair target zeros [rad/sec]
$\omega_{cmd}$	Command model frequency [rad/sec]
$\omega_{inv}$	Inverse model frequency [rad/sec]
$\omega_{sp}$	Short-period frequency [rad/sec]
$\phi$	Bank angle [rad]
$\tau$	Time delay [sec]
$\tau_n$	Normal acceleration transfer function equivalent time delay [sec]
$\tau_q$	Pitch rate transfer function equivalent time delay [sec]
$\tau_{cmd}$	Command time delay [sec]
$\theta$	Pitch attitude [deg, rad]
$\theta_{DB}$	Pitch attitude dropback [deg]
$\zeta$	Damping ratio [-]
$\zeta_\alpha$	LQR output shaping function damping of complex-pair target zeros [-]
$\zeta_{cmd}$	Command model damping [-]
$\zeta_{inv}$	Inverse model damping [-]
$\zeta_{sp}$	Short-period damping [-]
$a$	LQR output shaping function real zero [rad/sec]
$g$	Acceleration due to gravity [ft/sec <sup>2</sup> ]
$J_{LOES}$	LOES fit cost
$J_{MF}$	Model following cost
$K$	Control law gain
$K_n$	Normal acceleration transfer function gain [g/deg-elev]
$K_q$	Pitch rate transfer function gain [rad/sec/deg-elev]
$K_{stk}$	Stick gain [g/lb]
$K_u$	Speed error gain [g/kt]
$M_\alpha$	Dimensional pitch stiffness derivative [1/sec]
$M_{\delta_e}$	Dimensional pitch rate control derivative [rad/sec <sup>2</sup> /deg – elev]
$n/\alpha$	Steady-state normal acceleration change per unit change of angle-of-attack [g/rad]
$n_z$	Normal acceleration [g]
$n'_z$	Normal load factor at the ICR [g]
$n_z u, n_z + u$	Normal acceleration plus speed error [g]
$n_{zcmd}$	Commanded normal load factor [g]
$Q$	LQR output shaping function weight [-]
$q$	Pitch rate [deg/sec, rad/sec]
$q_{pk}$	Peak pitch rate [deg/sec]
$q_{ss}$	Steady-state pitch rate [deg/sec]
$s$	Laplace variable
$T_{\theta_2}$	Short-term numerator time constant in the pitch rate response to longitudinal control, also known as flight path-attitude lag [sec]
$u$	Longitudinal velocity [ft/sec]
$u_{filt}$	Filter input
$V$	True airspeed [ft/sec]
$x_{ICR}$	Distance from center of gravity to instantaneous center of rotation [ft]
$y$	LQR output shaping function [-]
$y_{filt}$	Filter output
$Z_{\delta_e}$	Dimensional vertical force control derivative [ft/sec <sup>2</sup> /deg – elev]
CAP	Control Anticipation Parameter [1/g-sec <sup>2</sup> ]
CG	Center of Gravity
DRB	Disturbance Rejection Bandwidth
DRP	Disturbance Rejection Peak
EMF	Explicit Model Following

ICR	Instantaneous Center of Rotation
KTAS	Knots True Airspeed
LOES	Lower Order Equivalent System
LQR	Linear-Quadratic Regulator
MAC	Mean Aerodynamic Chord
OLOP	Open Loop Onset Point
PIO	Pilot Induced Oscillation

## I. Introduction

SEVERAL comprehensive compendiums of flight control design experience and lessons learned emphasize the importance of meeting multi-tier handling qualities and flight control criteria for improved safety (e.g. RTO,<sup>1</sup> Pratt<sup>2</sup>). The RTO report<sup>1</sup> mentions this approach as a best practice for flight control design and suggests that pilot induced oscillations (PIO) could be avoided in the design phase by exploiting handling qualities criteria to design for good handling qualities. It also suggests using supplementary criteria where necessary in addition to the military specifications. Many of these supplementary criteria, such as the bandwidth criteria<sup>3</sup> and the Gibson criteria,<sup>4</sup> have been incorporated into the latest version of military specification MIL-STD-1797B.<sup>5</sup> More recently, Balas and Hodgkinson<sup>6</sup> also referred to different tiers of requirements, or alternate criteria, used to supplement the equivalent modal parameters.

This paper applies these lessons to longitudinal control laws widely used in industry, using a model of a small business jet in nonterminal flight phase. The control laws used in this analysis are similar to the ones presented by Gangsaas, et al.<sup>7</sup> Furthermore, the linear-quadratic regulator (LQR) design method using target zeros employed by Gangsaas, et al,<sup>7</sup> was utilized in a preliminary design phase to initialize control law gain values. The gains were then directly optimized to satisfy the handling qualities and flight control requirements using a multi-objective parametric optimization algorithm. This two step process eliminated manual tuning of the LQR performance parameters and produced excellent initial conditions for the optimization. This resulted in the ability to optimize an entire gain schedule in a matter of hours with no manual tuning.

The paper first describes the aircraft for which this control system is designed. Next, a detailed description of the control laws is given, including a discussion of which elements in the control laws can be modified between flight condition, or scheduled. After a brief description of the Control Designer's Unified Interface (CONDUIT<sup>®</sup>), the software used for control law optimization in this study, a description of the handling qualities specifications used is given. Then, the optimization strategy is discussed, including a detailed description of how LQR is used to initialize the gain values. Finally, the results are presented, first for one flight condition, and then for the entire gain schedule, followed by conclusions.

## II. Aircraft Model

THE aircraft used in this study is a light business jet similar to the Cessna CitationJet 1 (CJ1), or Model 525, shown in Figure 1. It is a twin turbofan-powered business jet which can carry three to nine passengers. It has a maximum take-off weight (MTOW) of 10,700 lbs, a cruise speed of 389 KTAS, a maximum range of 1,300 nm, and a service ceiling of 41,000 ft. For this study, it is assumed that the elevator is driven by a hydraulic actuator, with a full authority fly-by-wire control system.

In order to produce meaningful analyses and develop a good control system, a comprehensive full flight envelope model of the aircraft dynamics is necessary. In this case, linear models of the aircraft at different Mach, flight altitude, weight, and center of gravity (CG) combinations were estimated using DARcorporation Advanced Aircraft Analysis software.<sup>8</sup> Sixty-six different Mach and altitude combinations were considered, and at each of those design points, 13 different weight and CG combinations were considered, for a total of over 850 models. All models are for a flaps-up, gear-up cruise configurations. Figure 2(a) shows the different Mach and altitude combinations, as well as the aircraft flight envelope.<sup>9</sup> Figure 2(b) shows the different weight and CG combinations, as well as the aircraft weight-CG envelope.<sup>9</sup> Several weight/CG configurations which are outside the envelope were used in this analysis in order to design the control laws for additional robustness.

As the control law gains will not be scheduled with weight or CG, for the sake of simplicity, each Mach/altitude combination is treated as a design point with a nominal loading configurations (weight =



Figure 1. Typical light business jet—Cessna CitationJet 1 (CJ1), or Model 525.

8500 lbs, mid-CG location) marked as “Nominal” on Figure 2(b), and two off-nominal weight and CG configurations, marked as “Light” and “Heavy” on Figure 2(b). Figures 3(a) and 3(b) show the range of pitch rate and normal acceleration frequency responses for all weight and CG configurations (grey patches) at one point design (Mach 0.3, Sea Level). Highlighted on the plots are the responses for the nominal loading configurations and two off-nominal loading configurations (“Light”-weight = 6000 lbs, aft-CG and “Heavy”-weight = 10,800 lbs, mid-CG), which span the range of variations in the pitch rate and normal acceleration responses for all the weight/CG configurations. These off-nominal loading configurations will be used in evaluating certain specifications to ensure control law stability and performance robustness to changes in weight and CG.

In addition to the variation between the nominal and off-nominal loading configurations, the variation due to Mach/altitude must be considered for the purpose of gain scheduling. Figures 4(a) and 4(b) show variations in the bare-airframe short-period frequency and damping of the nominal weight/CG configuration as a function of Mach and inverse dynamic pressure. The plots are shown as a function of  $40/\bar{q}$  instead of  $1/\bar{q}$  to scale the x-axis around 0-1. The short-period frequency increases with increasing dynamic pressure (decreasing  $40/\bar{q}$ ) and is well grouped for different Mach values. Conversely, the short-period damping increases both with increasing dynamic pressure (decreasing  $40/\bar{q}$ ) and with decreasing Mach number. Additional examples of the variations of stability and control derivatives with loading and flight conditions are presented in Tischler and Remple.<sup>10</sup> Due to these variations with both dynamic pressure and Mach, both parameters will be used to schedule the control law gains.

### III. Control Laws

THE control law architecture used in this study is based on that presented by Gangsaas, et al,<sup>7</sup> shown in simple form in Figure 5. The control laws are “ $n_z u$ ”-command, i.e. a combination of normal acceleration and speed error ( $n_z + Ku$ ). As shown by Gangsaas, et al, commanding  $n_z + Ku$ , as opposed to pure  $n_z$ , not only re-introduces the phugoid mode back into the aircraft response, but also gives speed stability and preserves the static stability gradients of column force per g and column force per knot, as required by FAA Federal Aviation Regulation (FAR) 25.173(c)<sup>11</sup> and MIL-STD-1797B.<sup>5</sup> Furthermore, Gangsaas, et al, explain that the feed-forward path in Figure 5, comprised of the direct column to elevator path, as well as the second-order pre-filter, is adjusted to meet the handling qualities requirements, while the feedback path, comprised of angle-of-attack and angle-of-attack rate, is used to meet the short-period frequency and damping requirements.

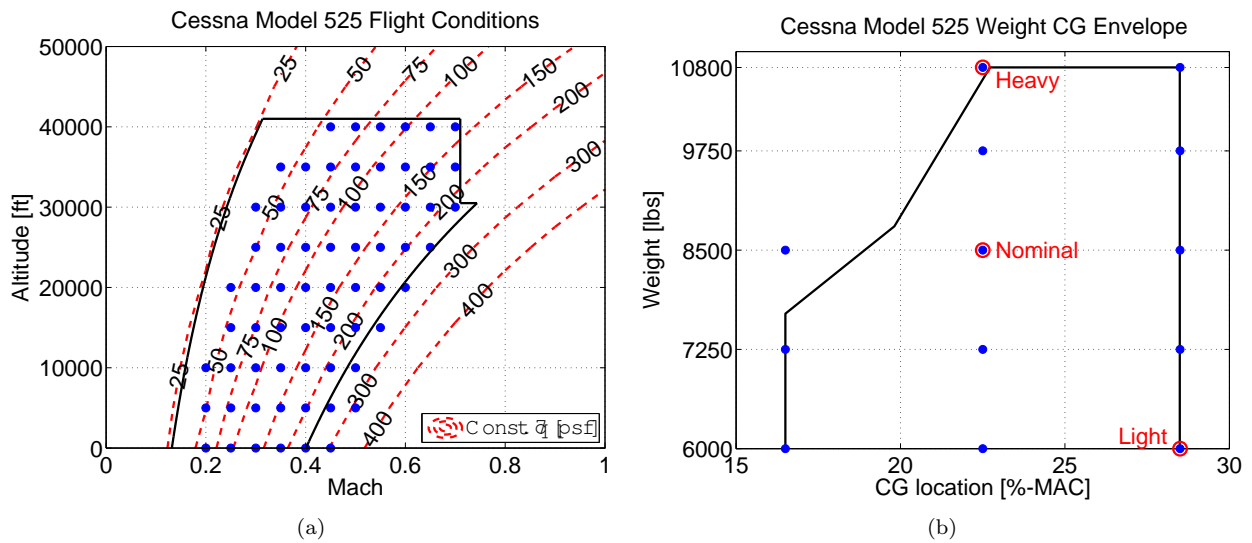


Figure 2. Aircraft (a) flight and (b) loading conditions and envelopes.

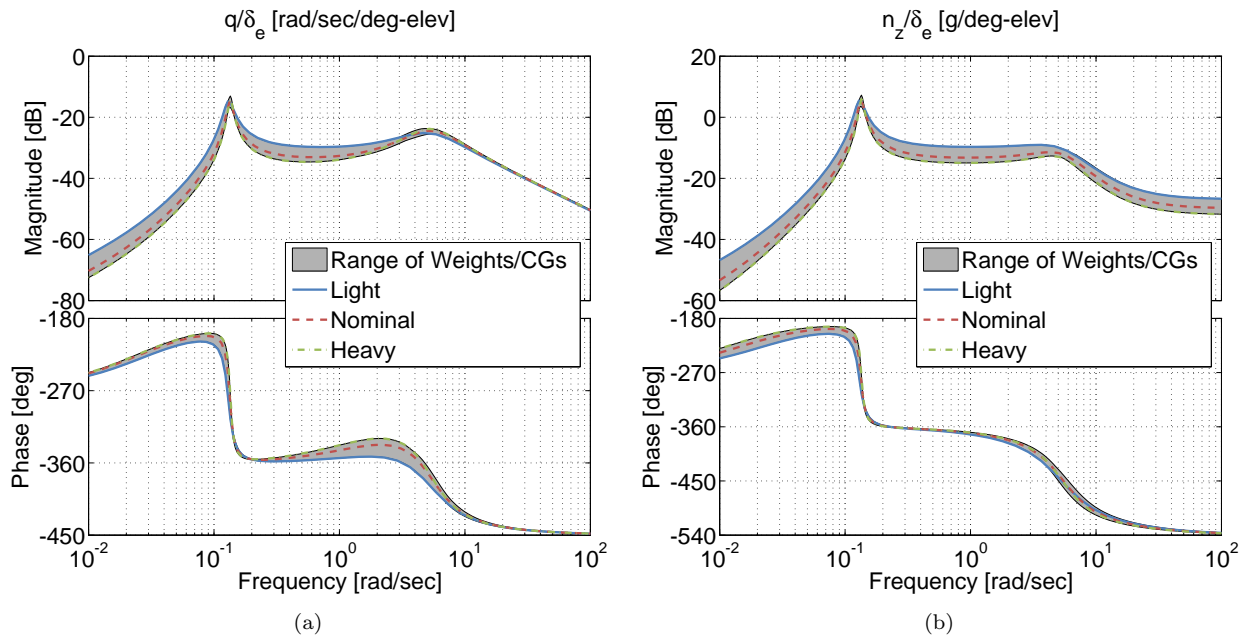


Figure 3. Range of (a) pitch rate and (b) normal acceleration responses across the range of weight and CG configurations (Mach 0.3/Sea Level flight condition).

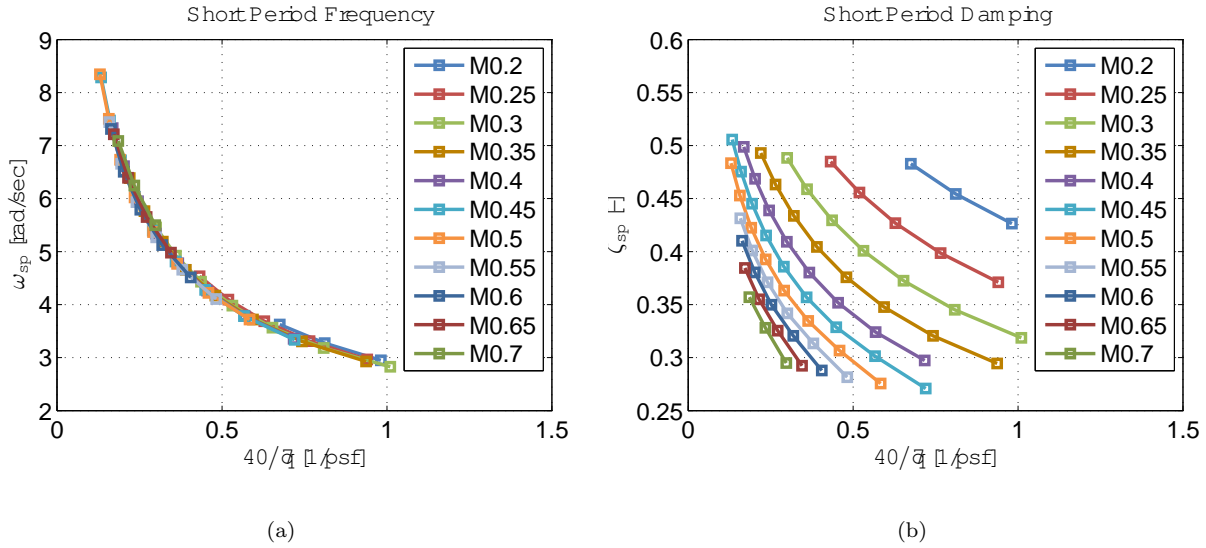


Figure 4. Variations in bare-airframe short-period (a) frequency and (b) damping with Mach and inverse dynamic pressure (Nominal weight/CG).

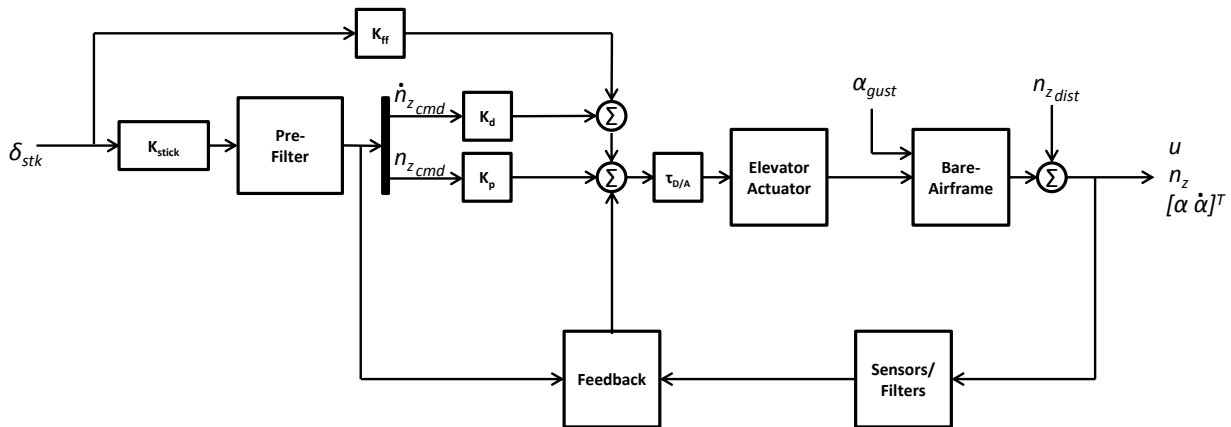


Figure 5. Schematic of typical longitudinal control law block diagram (based on Gangsaas, et al<sup>7</sup>).

The control laws shown in Figure 5 can be seen as very similar to the explicit model following (EMF) control law architecture,<sup>12</sup> which is often used in rotorcraft control and is shown in Figure 6. It is helpful to explore these similarities because EMF control laws assure that the end-to-end response follows the desired lower-order command model. This is useful for gain scheduling of the command model, as is done here and described in Section III.A.1. Moreover, a lower-order end-to-end response is desired, both for good handling qualities,<sup>7</sup> and to ensure that the LOES specifications, described in Section V, accurately predict the handling qualities of the aircraft.

Figure 7 shows the control law block diagram which is used in this study, and illustrates the link between the original block diagram of Figure 5 and the EMF block diagram of Figure 6. The Pre-Filter block in Figure 7 is used as the Command Model, which is covered in more detail in Section III.A.1. The feed-forward gains  $K_p$ ,  $K_d$ , and  $K_{ff}$  take the place of the Inverse Model block in the EMF control laws. Section VI.A will describe how these three gains can be used to exactly construct a second-order inverse model of the aircraft,

in order to achieve the full benefits of an EMF controller with the architecture used here.

The addition of the command delay block ( $\tau_{cmd}$  in Figure 7), which was not used in the original block diagram of Figure 5, was done to enhance the control law's model following capabilities by synchronizing the command model and aircraft responses. The benefits of this delay are shown in Section III.A.2.

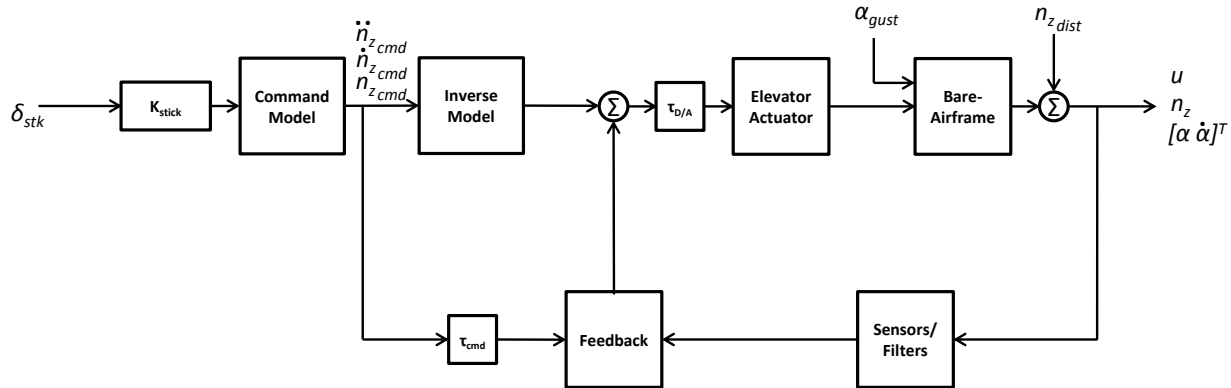


Figure 6. Schematic of explicit model following control law block diagram.

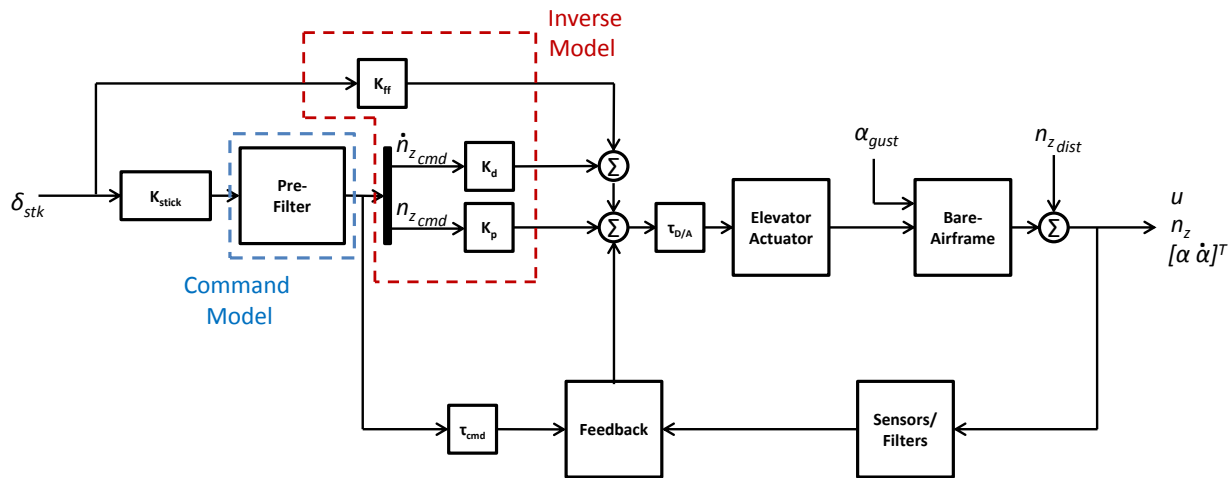


Figure 7. Schematic of the control law block diagram optimized in this study.

The remainder of this section will be broken down into the Design Parameters and Set Parameters of the block diagram. Design parameters are those that are determined either by hand tuning or through optimization, and are different for each flight condition. Set parameters, are those which do not change with flight condition, and are frozen throughout the aircraft flight envelope.

## A. Design Parameters

### 1. Feed-Forward

The first component of the feed-forward section of the control laws is the command model, sometimes referred to as a pre-filter. The command model is second-order, and represents the desired dynamics:

$$\frac{n_{z_{cmd}}}{\delta_{stk}} = \frac{\omega_{cmd}^2}{s^2 + 2\zeta_{cmd}\omega_{cmd}s + \omega_{cmd}^2} \quad (1)$$

Where,

$\zeta_{cmd} = 1.0$  to provide a well damped response, and  
 $\omega_{cmd} = \omega_{sp}$  to retain the good inherent short-period frequency of the bare-airframe aerodynamic design and to not overdrive the actuators.

Note that the short-period frequency is selected for the nominal weight/CG configuration at each flight condition. As shown in Figure 7, the commanded normal acceleration,  $n_{z_{cmd}}$ , and derivative of normal acceleration,  $\dot{n}_{z_{cmd}}$ , produced by the command model are fed directly to the elevator through gains  $K_p$  and  $K_d$ , respectively. There is also a direct stick to elevator actuator gain,  $K_{ff}$ .

Column force per commanded g is set by a gain on the pilot stick input given by:

$$K_{stick} = \frac{1}{50 \text{ lb/g}} \quad (2)$$

Column force per knot is set by passing the speed error signal through the following gain, as shown later in Figure 10:

$$K_u = \frac{1/6 \text{ lb/kt}}{50 \text{ lb/g}} = 0.0033 \text{ g/kt} \quad (3)$$

thus generating a g demand per knot of speed error which is summed with the commanded normal acceleration from the command model, generating the “ $n_z u$ ”-command. This gives the following stick gradients: 50 lb/g and 1/6 lb/kt.

## 2. Command Delays

Command delays, shown as the  $\tau_{cmd}$  block in Figure 7, are used to delay the commanded states by a time  $\tau_{cmd}$  before comparing them to the actual aircraft states. This synchronizes the commanded and actual states in time, before determining the error. The addition of command delays is typical in EMF control laws (Figure 6), and is done to account for higher-order dynamics and delays from the actuators, bare-airframe, sensors, filters, and flight control computer processing time that are not accounted for by the inverse model.<sup>12</sup> The command delays are calculated by breaking the feedback loops, and fitting a pure time delay to the phase difference between each command signal and its corresponding fed back aircraft response.

Accounting for this additional delay before comparing the commanded states with the actual states is useful to not overdrive the actuators. The addition of the command delays also reduces the amount of overshoot in the closed-loop end-to-end response with no added phase loss, which is shown for the normal acceleration response in the frequency domain in Figure 8 and in the time domain in Figure 9. The two figures also show that the addition of the command delays allow for better tracking of the commanded normal acceleration response, with less actuator activity (Figure 9).

## 3. Feedback

The feedback section of the control law (Feedback block in Figure 7) is shown in more detail in Figure 10. Feedback is used to minimize the error between the commanded normal acceleration and actual aircraft response. This is done with integral, proportional, and derivative paths.

For the integral path, the commanded normal acceleration,  $n_{z_{cmd}}$ , and speed error,  $u$ , are summed to generate the “ $n_z u$ ”-command,  $n_z u_{cmd}$ , signal. This signal is compared with the actual aircraft normal acceleration,  $n_z$ , and fed back through an integrator and integral gain,  $K_i$ , as shown in Figure 10.

For the proportional and derivative paths, the quantities fed back are complementary filtered angle-of-attack and angle-of-attack rate reconstructed from inertial measurements:

$$\dot{\alpha}_{inertial} = q + g \frac{\cos \phi \cos \theta \cos \alpha + \sin \theta \sin \alpha - n_z}{U} \quad (4)$$

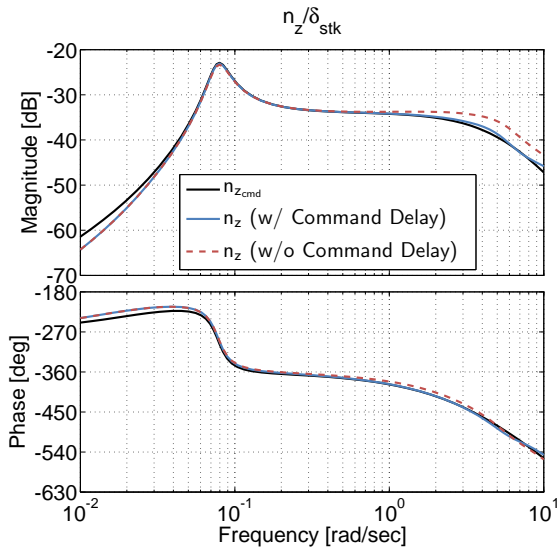


Figure 8. Effect of command delay on closed-loop response in the frequency domain.

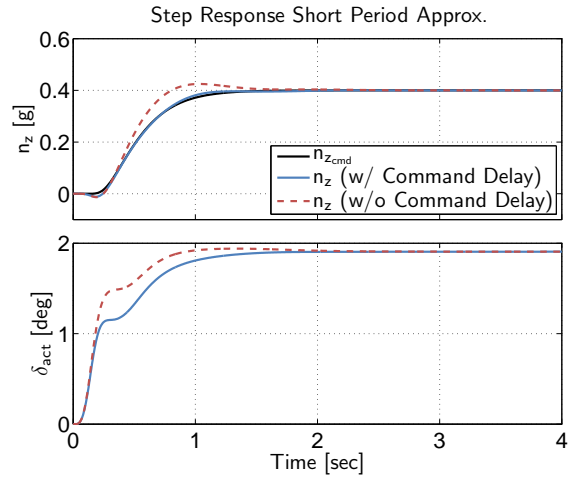


Figure 9. Effect of command delay on closed-loop response in the time domain.

In the short-term (frequency range of the short-period dynamics), angle-of-attack and normal acceleration have a constant shift in magnitude by gain  $\alpha_{nz}$ :

$$\alpha_{nz} = \frac{1}{n/\alpha} = \frac{g}{V} T_{\theta_2} \quad (5)$$

This gain is used to convert the commanded normal acceleration,  $n_{zcmd}$ , and the derivative of commanded normal acceleration,  $\dot{n}_{zcmd}$ , into commanded angle-of-attack,  $\alpha_{cmd}$ , and commanded angle of attack rate,  $\dot{\alpha}_{cmd}$ . Those commanded values are compared with the actual aircraft angle-of-attack and angle-of-attack rate, and the errors are fed back through gains  $K_\alpha$  and  $K_{\dot{\alpha}}$ , respectively, as shown in Figure 10.

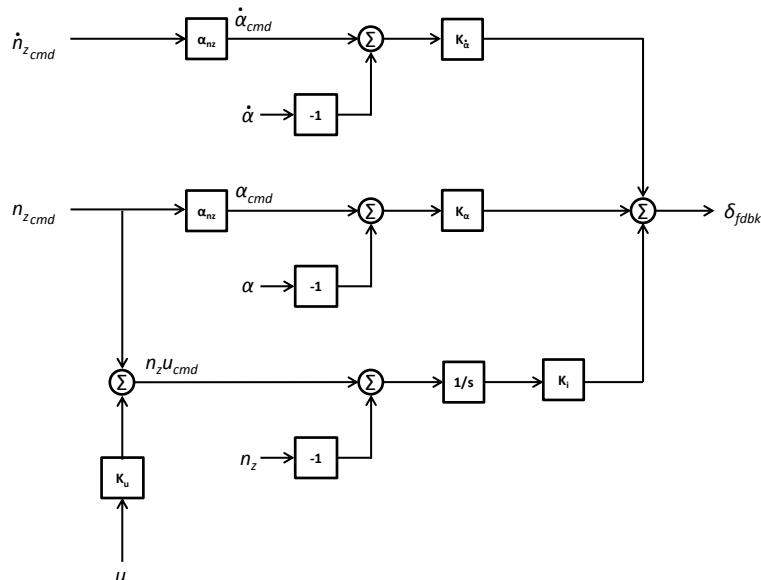


Figure 10. Schematic of the feedback block in the control law block diagram.

## B. Set Parameters

### 1. Actuator

For the system modeled, there is an elevator actuator represented as a second-order system with  $\omega_n = 22.6$  rad/sec,  $\zeta = 0.7$ , a position limit of  $\pm 15$  deg, and a rate limit of 36 deg/sec.

### 2. Sensors and Sample Delay

The digital-to-analog sample and hold delay is accounted for by a half time-step ( $\tau = 10$  msec) delay upstream of the elevator actuator for the assumed 50 Hz flight control computer (FCC).<sup>13</sup> Sensors are modeled as second-order systems with frequencies of  $\omega_n = 4.8$  Hz on angle-of-attack and airspeed, and  $\omega_n = 25$  Hz on pitch rate and attitude and on longitudinal and normal accelerations. Additionally, each sensor signal has a  $\tau = 20$  msec delay, to account for sampling skew and bus transport delays.

### 3. Filters

The stick input anti-aliasing filter is modeled as a first order 5 Hz lag.

Filters on the measured aircraft responses include a complementary filter on angle-of-attack using angle-of-attack rate reconstructed from inertial measurements, as shown in Equation 4.

The complementary filtered angle-of-attack,  $\alpha_{cf}$ , is built up such that:

$$\alpha_{cf} = \underbrace{\frac{s}{s^2 + 2\zeta_{cf}\omega_{n_{cf}}s + \omega_{n_{cf}}^2} \dot{\alpha}_{inertial}}_{\text{High-Frequency Contribution}} + \underbrace{\frac{2\zeta_{cf}\omega_{n_{cf}}s + \omega_{n_{cf}}^2}{s^2 + 2\zeta_{cf}\omega_{n_{cf}}s + \omega_{n_{cf}}^2} \alpha_{measured}}_{\text{Low-Frequency Contribution}} \quad (6)$$

Where,

$\dot{\alpha}_{inertial}$  is angle-of-attack rate reconstructed from inertial measurements (Equation 4),

$\alpha_{measured}$  is the measured angle-of-attack,

$\omega_{n_{cf}}$  is the complementary filter frequency, 0.25 rad/sec in this case, and

$\zeta_{cf}$  is the complementary filter damping, 0.7 in this case.

Figure 11 shows the contribution of reconstructed angle-of-attack,  $\alpha_{inertial}$ , and measured angle-of-attack,  $\alpha_{measured}$  to the complementary filtered angle-of-attack. As expected, the inertial and measured components sum to 1.0, as indicated by Equation 6 and Figure 11. Additionally, there is a similarly constructed complementary filter on true airspeed.

To properly capture all sources of the control law's phase lag, structural notch filters have also been included in the block diagram. In this example, the notch filters are used only in the angle-of-attack rate feedback signal,  $\dot{\alpha}_{inertial}$ . For the purposes of this analysis, it is assumed that the integration of the normal acceleration signal in the control laws, as well as the complementary filter on the angle-of-attack signal, provide inherent high-frequency attenuation, and therefore notch filters are not required for these signals. Sample structural mode notch filters for this class of aircraft could include notches at  $\omega_n = 5, 10,$  and  $15$  Hz, which have been used for the notch filters in this analysis. The damping ratio for the numerator and denominator notch filter terms are  $\zeta_{num} = 0.05$  and  $\zeta_{den} = 0.5$ , respectively, which set the depth and width of each filter. These notch filters are assumed for this control law and aircraft to provide aeroelastic stability, which requires 9 dB of gain margin from control law structural coupling.<sup>14</sup> However, an aeroelastic stability analysis that includes the coupled aircraft and structural dynamics is required for production control law design, but is out of scope for this analysis.

A lead-lag filter is also added downstream of the notch filters to help recover some of the phase loss associated with the notches. This was necessary in order to meet the damping ratio specification for some of the higher Mach flight conditions. The lead-lag filter was hand tuned using several of the corner cases of the flight envelope. The trade-off between the added phase lead at the cost of more high-frequency gain (which can reduce gain margin) from the lead-lag filter is shown in Figure 12. However, the notch filters with lead-lag still sufficiently reduce the broken-loop magnitude near the structural modes in order to meet the required 9 dB gain margin.

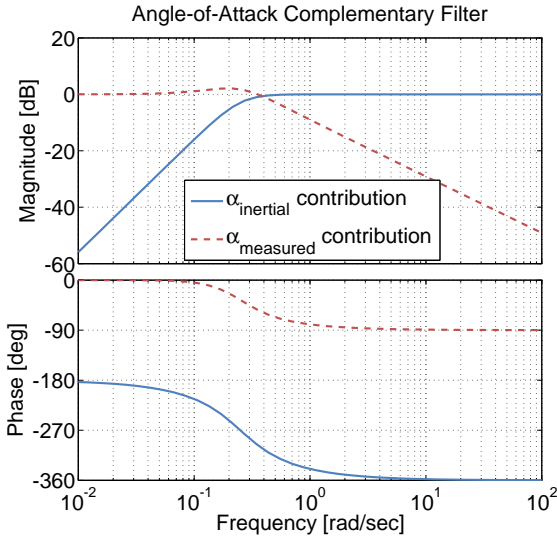


Figure 11. Complementary filtered angle-of-attack contributions.

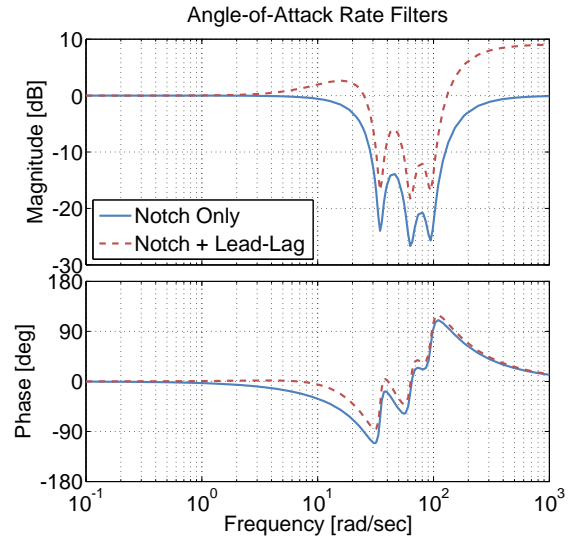


Figure 12. Filters on angle-of-attack rate.

#### 4. Turbulence, Gusts, and Disturbances

Finally, for the purpose of evaluating the control laws, a Dryden turbulence model,<sup>5</sup> as well as discrete 1-cosine angle-of-attack and speed gust models<sup>11</sup> have been integrated into the block diagram. These are included through an additional input to the bare-airframe state-space model, a  $B_{gust}$  matrix, which is comprised of only the aerodynamic terms (no inertial or gravity terms) of the bare-airframe state-space model  $A$  matrix. Disturbances in each response are summed into the output of the bare-airframe block.

## IV. Control Designer's Unified Interface

THE control laws described in the previous section were analyzed and optimized using the Control Designer's Unified Interface (CONDUIT<sup>®</sup>).<sup>15,16</sup> CONDUIT<sup>®</sup> is a commercial software tool developed by the U.S. Army Aeroflightdynamics Directorate in conjunction with the University Affiliated Research Center, University of California, Santa Cruz. It leverages MATLAB<sup>®</sup> to evaluate a Simulink block diagram against a defined set of stability, handling qualities, and performance specifications, and performs a multi-objective parametric optimization of user defined parameters in the block diagram (e.g. feedback gains) in order to meet those specifications, while minimizing the cost of feedback (actuator usage and noise sensitivity).

## V. Specifications

A comprehensive set of stability, handling qualities, and performance specifications was chosen to drive the optimization of the control laws. The handling qualities specifications are based on MIL-STD-1797B<sup>5</sup> and engineering judgement. The static stick gradients are based on the FAA requirements.<sup>11</sup> The required stability margin is based on the military specification for flight control systems, MIL-DTL-9490E.<sup>14</sup> The specifications were divided into two categories—First Tier and Second Tier specifications. First Tier specifications are key flight control and handling qualities requirements that drive the design optimization. They are evaluated at each iteration of the control law optimization and are guaranteed to be met for an optimized design. Second Tier specifications are those which are evaluated only at the end of the optimization. Because they are not evaluated during the optimization, due to computational time consideration, they are not always met. However, they are evaluated for the optimized design to ensure they are not grossly violated. There is generally sufficient overlap between the First Tier and Second Tier specifications, such that the Second Tier specifications are also met or are close to being met by the optimization process.

## A. First Tier Specifications

First Tier specifications are used to drive the optimizations and are divided into three constraint types in CONDUIT<sup>®</sup>. Specifications that ensure aircraft stability, such as the eigenvalue, stability margin, and Nichols margin specifications, are categorized as *hard constraints*. These specifications are met during the first phase of optimization, and cannot be violated in subsequent phases of the optimization.

The next subset of First Tier specifications contains the handling qualities specifications, which are categorized as *soft constraints* and are met during the second phase of optimization. These specifications include the lower order equivalent systems (LOES) specifications of MIL-STD-1797B: CAP,  $n/\alpha$ , short-period damping and frequency, and equivalent time delay. As this analysis was done for up-and-away flight conditions and a medium weight aircraft, the Category B, Class II-L boundaries were used for the MIL-STD-1797B LOES specifications.

In addition to those LOES specifications, three more LOES specifications were included in the optimization. Inclusion of the first additional LOES specification enforces the cost of the LOES fit to be  $J_{LOES} \leq 10$ . This ensures that the aircraft responds like a lower order system and that the parameters of the LOES fit accurately capture the closed-loop dynamics of the aircraft. The second additional LOES specification ensures that the short-period frequency of the LOES fit is within  $\pm 25\%$  of the bare-airframe short-period frequency. The inclusion of this specification prevents over driving of the actuators. The third additional LOES specification compares the value of  $T_{\theta_2}$  of the LOES fit and ensures that it is within  $\pm 50\%$  of the bare-airframe  $T_{\theta_2}$ . This preserves the good short-period response of the bare-airframe design, while allowing for improvement of the short-period damping.

The LOES fit used here is a simultaneous fit of the pitch rate response to pitch stick input and normal acceleration at the instantaneous center of rotation (ICR) response to pitch stick input. A short-period approximation is used over the frequency range of 0.5-12 rad/sec, and the LOES transfer functions are given below:

$$\frac{q}{\delta_{stk}} = \frac{K_q(s + 1/T_{\theta_2})e^{-\tau_q s}}{s^2 + 2\zeta_{sp}\omega_{sp}s + \omega_{sp}^2} \quad (7)$$

$$\frac{n'_z}{\delta_{stk}} = \frac{K_n e^{-\tau_n s}}{s^2 + 2\zeta_{sp}\omega_{sp}s + \omega_{sp}^2} \quad (8)$$

Note that the normal acceleration at the ICR, and not at the CG, is required for this fit to eliminate the zeros in the  $n_z/\delta_{stk}$  response of Equation 8. The distance between the CG and ICR is given by:<sup>17</sup>

$$x_{ICR} = \frac{Z_{\delta_e}}{M_{\delta_e}} \quad (9)$$

The normal acceleration at the ICR can then be calculated as:

$$n'_z = n_z + \frac{x_{ICR}}{g} \dot{q} \quad (10)$$

The remaining handling qualities specifications do not require a LOES fit. The model following cost specification compares the closed-loop normal acceleration frequency response with the frequency response of the commanded normal acceleration. A cost function is computed based on the difference in the magnitude and phase of the responses, similar to a LOES cost. The comparison is done over the frequency range of 0.1 rad/sec up to 1.5 times the bare-airframe short-period frequency. This is the frequency range where it is desired to have the aircraft response track the command model, which has a frequency equal to the bare-airframe short-period frequency. A cost of  $J_{MF} \leq 50$  was enforced for the nominal aircraft configuration, whereas a cost of  $J_{MF} \leq 100$  was enforced for off-nominal configurations. This is consistent with guidelines for system identification of lower order equivalent models.<sup>10</sup>

The stick gains on the normal acceleration and calibrated airspeed are evaluated from the low-frequency gains of those responses (note that a short-period approximation of the bare-airframe is used for the normal acceleration response). The stick gains are then compared with the prescribed stick gradients defined in Section III.A.1, to assure that they are within  $\pm 2.5\%$ .

The next specification is the eigen-damping specification. This specification evaluates the damping ratio of all closed-loop eigenvalues within a specified frequency range and compares them to the minimum required value. The minimum damping ratio requirement is a function of frequency:

$$\zeta \geq \begin{cases} 0.04 & \omega_n < 0.5 \text{ rad/sec} \\ 0.4 & 0.5 \leq \omega_n < 20 \text{ rad/sec} \\ 0.25 & \omega_n \geq 20 \text{ rad/sec} \end{cases} \quad (11)$$

Meeting this specification ensures that the phugoid mode damping is above the  $\zeta_{ph} \geq 0.04$  requirement<sup>5</sup> and that there are no lightly damped high-frequency modes.

The Open Loop Onset Point (OLOP) specification<sup>18</sup> is included to evaluate the control law's susceptibility to Category II Pilot Induced Oscillations (PIOs). Category II PIOs are characterized by rate or position limiting. The OLOP specification examines actuator rate limiting, which has been the cause of several high profile accidents.<sup>18</sup> Linear analysis methods ignore the non-linear effects of position and rate limiting. However, the OLOP specification is based on frequency domain describing function concepts, and is useful to include in the design process to not push the design beyond the limits of the real aircraft.

Additional First Tier specifications concerned with ride quality are disturbance rejection bandwidth and peak.<sup>19</sup> Disturbance rejection is assessed by evaluating the loop sensitivity function, i.e.:

$$\frac{n_z}{n_{z_{dist}}} = \frac{1}{1 + GH} \quad (12)$$

In this case, disturbance rejection was assessed for the normal acceleration at the CG response, as shown in Equation 12. Disturbance rejection bandwidth (DRB) is defined as the frequency where the magnitude curve of the sensitivity function frequency response crosses the -3 dB line. This is the frequency below which the control system can adequately reject disturbances and is a measure of the quickness of the system to recover from a disturbance. Disturbance rejection peak (DRP) is the peak magnitude of the sensitivity function frequency response, and is a good measure of response overshoot for disturbance inputs. Figure 13 shows an example disturbance rejection response with its associated DRB and DRP.

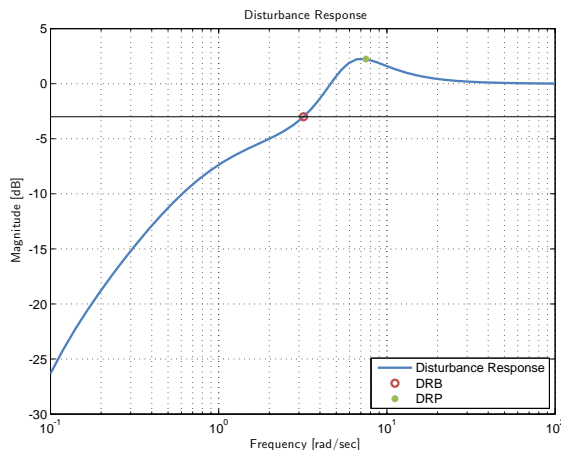


Figure 13. Example disturbance rejection bandwidth and peak.

A minimum crossover frequency specification is included in the optimization, as well. This specification ensures that the frequency response broken at the elevator actuator has a crossover frequency  $\omega_c \geq 2.5$  rad/sec. Setting the minimum crossover frequency is an alternate way to ensure the control system is robust to off-nominal configurations, rather than explicitly including many off-nominal models in the evaluation of every specification, which is computationally intensive for optimization. It is especially useful in model following control law architectures such as this one, since most of the other handling qualities specifications can be met with a properly tuned command model and little feedback. Preliminary design, rules of thumb (e.g. Tischler, et al<sup>16</sup>), company history, or a trade-off study (as described in Section VII.B) are good ways to determine the value for minimum crossover.

Two First Tier time-domain specifications are included. They are the pitch attitude dropback<sup>20,5</sup> specification and a gust response specification. The gust response specification evaluates the normal acceleration response of the aircraft to a 1-cosine angle-of-attack gust, given by:

$$\alpha_{gust} = \frac{K_g}{2} (1 - \cos(\omega_g t)), 0 \leq t \leq 2\pi/\omega_g \quad (13)$$

Where,

$$K_g = 5 \text{ deg, and}$$

$$\omega_g = \omega_{sp}.$$

Meeting this specification ensures that the resulting normal acceleration response has a second peak that is less than or equal in magnitude to the first peak, as shown later in Figure 27. This gust response specification aims at increasing the short-period damping in order to reduce wing loads. The reduction of the first peak of the normal acceleration response is not practical, because the control system cannot react quickly enough. There is a trade-off however, since increasing the short-period damping normally results in higher activity of the control (i.e. crossover frequency in the elevator loop), which results in increased torsion load on the horizontal tail. Therefore, gust load alleviation is normally a compromise between several loads at several stations on the aircraft.

The final group of First Tier specifications are used for performance optimization. These are categorized as *summed objectives*, and CONDUIT<sup>®</sup> minimizes these after all other specifications have been met. In this case, the two specifications included in this category are crossover frequency and root mean squared (RMS) actuator displacement for an angle-of-attack gust input. Minimizing crossover frequency and actuator usage has many benefits including minimizing potential for spillover of control energy to high-frequency modes that can excite structural dynamics, improved stability margin robustness to uncertainty in aircraft dynamics, minimizing closed-loop sensitivity to noise, and minimizing potential actuator saturation and susceptibility to PIO. These specifications are referred to as the “cost of feedback” specifications. The best design is the one that meets all of the stability and handling qualities requirements with the minimum cost of feedback.<sup>16</sup> Note that the crossover frequency cannot be reduced below the 2.5 rad/sec that is enforced by the minimum crossover frequency soft objective requirements.

## B. Second Tier Specifications

Second Tier specifications are checked at the end of the design, but not evaluated during the optimization, in order to reduce optimization times. These specifications include the pitch attitude and flight-path bandwidth specifications from MIL-STD-1797B. In addition, two Category I PIO specifications are included<sup>1</sup>—the Neal Smith and Gibson Phase Rate criteria.

These specifications are not guaranteed to be met for the optimized design, but sufficient overlap between these specifications and the First Tier specifications generally ensures that they are met. When Second Tier specifications are not met in the design process, they can be moved to the First Tier and used to drive the optimization to ensure they are met. Similarly, when First Tier specifications are found to not drive the design, they can be moved to the Second Tier to minimize computation time.

## C. Specification Summary

Table 1 lists the full set of First Tier and Second Tier specifications, as well as a brief description and source for each. The table also shows the weight/CG configurations used to evaluate each specification, which is described in more detail in Section VI.

**Table 1. Optimization Specifications**

Constraint	Spec Name	Description (Motivation)	Domain *	Source	Config. **	
<i>First Tier</i>						
Hard	EigLcG1	Eigenvalues in L.H.P. (Stability)	-	Generic	N	
	StbMgG1	Gain Phase Margin broken at elevator (Stability)	F	MIL-DLT-9490E	L,N,H	
	NicMgG1	Nichols Margins broken at elevator (Stability)	F	GARTEUR	L,N,H	
Soft	CapPiL2	CAP (short-period) (HQ)	L	MIL-STD-1797B	N	
	FrqSpL5	$\omega_{sp}$ vs $n/\alpha$ (HQ)	L	MIL-STD-1797B	N	
	TdlPiL1	Equivalent Time delay (HQ)	L	MIL-STD-1797B	N	
	FrqSpC1	$\omega_{sp} \pm 25\%$ open-loop (Act. Activity)	L	Generic	N	
	FrqTtC1	$T_{\theta_2} \pm 50\%$ open-loop (HQ, Act. Activity)	L	Generic	N	
	CosLoG1	Max LOES Cost ( $J \leq 10$ ) (HQ)	L	Generic	N	
	FspGsL1	Stick force per g $\pm 2.5\%$ stick gain (HQ)	F	Generic	N	
	FspKtL1	Stick force per kt $\pm 2.5\%$ stick gain (HQ)	F	Generic	N	
	ModFoG2	Command model following cost (HQ)	F	Generic	L,N,H	
	EigDpG1	Eigenvalue Damping (HQ, Loads)	-	Generic	N	
	OlpOpG1	Open Loop Onset Point (PIO)	F	DLR	N	
	DrpPiL1	Pitch dropback (HQ)	T	MIL-STD-1797B	L,N,H	
	GstRpG1	Angle-of-attack gust response (Loads)	T	Generic	N	
	DstBwG1	Dist. Rej. Bandwidth (Loads, Ride Quality)	F	ADS-33E	N	
	DstPkG1	Dist. Rej. Peak (Loads, Ride Quality)	F	ADS-33E	N	
	CrsMnG1	Minimum $\omega_c \geq 2.5$ rad/sec (Robustness)	F	Generic	N	
	Summed	CrsLnG1	Crossover Frequency (Act. Activity)	F	Generic	N
	Obj.	RmsAcG1	Actuator RMS (Act. Activity)	F	Generic	N
<i>Second Tier</i>						
Check Only	BnwPiL4	Bandwidth, phase delay (HQ)	F	MIL-STD-1797B	-	
	BnwFpL1	Transient flight-path response (HQ)	F	MIL-STD-1797B	-	
	NsmPiL1	Neal Smith (PIO)	F	AFFDL-TR-70-74	-	
	GibPiL1	Gibson phase rate (PIO)	F	AGARD-CP-508	-	
	NicMgG1	Nichols Margins broken at sensors (Stability)	F	GARTEUR	-	

\* F = Frequency domain specification, T = Time domain specification, L = LOES specification

\*\* N = Nominal weight/CG configuration only, L,N,H = Light, Nominal, and Heavy weight/CG configurations

## VI. Optimization Strategy

At each Mach/altitude flight condition, a multi-model point optimization was performed. The multi-model optimization includes off-nominal models (marked as “Light” and “Heavy” on Figure 2(b)) with variations in weight and CG at each Mach/altitude flight condition. Therefore, the multiple models used are each at the same flight condition, but with a different aircraft weight and CG position. As shown in Table 1, the off-nominal models were used to evaluate the stability and Nichols margin specifications. Additionally, the model following specification was evaluated for the off-nominal models using a relaxed boundary of  $J_{MF} \leq 100$ , instead of the boundary for the nominal model of  $J_{MF} \leq 50$ . Finally, the time domain dropback specification was evaluated for both the nominal and off-nominal models.

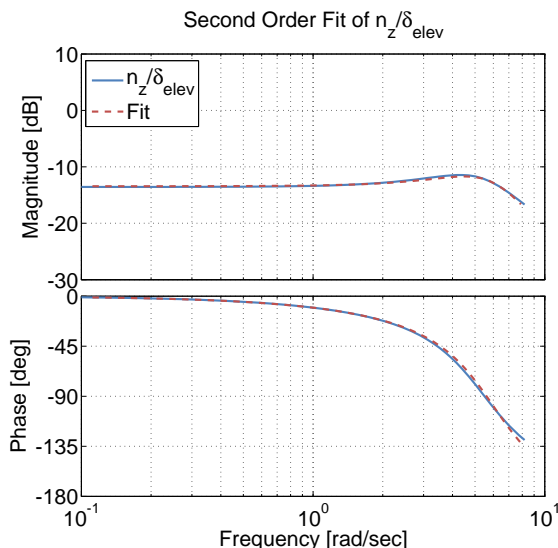
### A. Feed-Forward Gains

As described in Section III, the control laws used in this study, shown in Figure 7, are very similar to explicit model following control laws, shown in Figure 6. The difference between the control architecture used in this study and model following control laws is that the feed-forward gains  $K_p$ ,  $K_d$ , and  $K_{ff}$  take the place of the Inverse Model. However, these three gains can be used to exactly construct a second-order inverse model of the aircraft. The inverse model is determined by fitting a second-order transfer function model:

$$\frac{n_z}{\delta_{elev}} = \frac{K_{inv} e^{-\tau_{inv} s}}{s^2 + 2\zeta_{inv} \omega_{inv} s + \omega_{inv}^2} \quad (14)$$

to the short-period approximation of the bare-airframe normal acceleration response, and then inverting it.

The fit is done over a frequency range from 0.1 rad/sec up to 1.5 times the bare-airframe short-period frequency. Figure 14 shows the short-period approximation of the bare-airframe normal acceleration response for one of the flight conditions, as well as the transfer function fit. Equation 15 shows the transfer function and excellent fit cost.



$$\frac{n_z}{\delta_{elev}} = \frac{7.532}{[0.4615, 5.949]} e^{(-0.0226s)} \quad (15)$$

0.1 - 8.184 rad/sec, Cost = 1.327

Figure 14. Inverse model fit of normal acceleration response (Mach 0.3/Sea Level flight condition; Nominal weight/CG).

Once the parameters of the inverse model are known, they can be used along with the command model parameters to determine values for the three feed-forward gains:

$$K_p = (\omega_{inv}^2 - \omega_{cmd}^2)/K_{inv}\omega_{inv}^2 \quad (16)$$

$$K_d = (2\zeta_{inv}\omega_{inv} - 2\zeta_{cmd}\omega_{cmd})/K_{inv}\omega_{inv}^2 \quad (17)$$

$$K_{ff} = \omega_{cmd}^2/K_{inv}\omega_{inv}^2 \quad (18)$$

Note that since  $\zeta_{cmd}$  is set to equal 1.0, which is larger than the inverse model damping for all cases, the feed-forward gain  $K_d$  is negative.

## B. Feedback Gains

Feedback gains are optimized by CONDUIT<sup>®</sup> to meet the specifications, while minimizing actuator RMS and minimizing crossover frequency as far down to 2.5 rad/sec as the other specifications will allow. To increase convergence speed, it is important to have a good initial guess of the feedback gain values, especially when optimizing a large number of cases for an entire gain schedule. Initial values for the feedback gains are determined in preliminary design using the LQR method employed by Gangsaas, et al,<sup>7</sup> which will be described here in detail.

The first step in the LQR optimization is to generate a synthesis model. The synthesis model includes the aircraft dynamics, as well as the actuator and command model dynamics and an output shaping function.

Beginning with the three degree of freedom model of the bare-airframe rigid-body dynamics ( $x = [\alpha \ u \ q \ \theta]^T$ ), the actuator dynamics are added to the system. The actuator is modeled as a second order system with  $\omega_n = 22.6$  rad/sec,  $\zeta = 0.7$ , and results in the following state vector:  $x = [\alpha \ u \ q \ \theta \ \delta_{act} \ \dot{\delta}_{act}]^T$ . Next, a change of variable is made transforming the pitch rate state to angle-of-attack rate using a similarity transformation ( $x = [\alpha \ u \ \dot{\alpha} \ \theta \ \delta_{act} \ \dot{\delta}_{act}]^T$ ).

The command model, shown in Equation 1, is then included in the synthesis model. In addition to the two states of the command model, an integral error state is added given by:

$$\int err = \int (\alpha_{nz}n_{z_{cmd}} - \alpha) \quad (19)$$

The final state vector is then:  $x = [\alpha \ u \ \dot{\alpha} \ \theta \ \delta_{act} \ \dot{\delta}_{act} \ n_{z_{cmd}} \ \dot{n}_{z_{cmd}} \ \int err]^T$

The second component of the synthesis model is the output shaping function. The shaping function, given by:

$$y = \frac{(s + a)(s^2 + 2\zeta_\alpha\omega_\alpha s + \omega_\alpha^2)}{s} \alpha \quad (20)$$

is weighted by the LQR algorithm. It sets target zeros close to the locations of the desired closed-loop poles, or desired short-period and phugoid dynamics. In this case, a third order shaping function on angle-of-attack is used, where  $a$ ,  $\zeta_\alpha$ , and  $\omega_\alpha$  set the target zeros. Generally, the target zeros are treated as tuning knobs, and would be varied accordingly for each design point. However, in this case, since the LQR approach is used to initialize the feedback gains, the target zeros are fixed for all cases at:

$$a = \omega_{sp} \quad (21)$$

$$\omega_\alpha = \omega_{sp} \quad (22)$$

$$\zeta_\alpha = 0.85 \quad (23)$$

Where,

$\omega_{sp}$  is the short-period frequency of the nominal weight/CG bare-airframe at each flight condition.

With the target zeros fixed, the remaining tuning knob becomes the LQR weighting on the shaping function,  $Q$ . Since there is one shaping function used here,  $Q$  reduces to a scalar. The LQR solution then gives the feedback gain from each of the synthesis model states to the elevator (e.g.  $K_\alpha$ ,  $K_{\dot{\alpha}}$ , etc.). Note that the resulting feedback gains on the actuator states are generally very small and are dropped. In this example, the gains on airspeed and pitch attitude were very small and dropped as well, although it might sometimes be necessary to include a second shaping function on the phugoid states, in order to include airspeed or pitch attitude feedback. This is a useful aspect of the LQR preliminary design phase as it provides a good indication of which feedback gains should be included in the optimization and which gains are not needed to meet the specifications. This can also be determined after running the optimization by performing a sensitivity analysis in CONDUIT<sup>®</sup>, which is discussed later in Section VII.A.

The integral gain on the “ $n_z u$ ”-error is derived by:

$$K_i = \alpha_{nz} * K_{f_{err}} \quad (24)$$

Where  $K_{f_{err}}$  is the feedback gain on the  $\int err$  state, generated by the LQR algorithm.

Beginning with a small value for  $Q$ , the crossover frequency of the bare-airframe short-period dynamics with the LQR feedback gains  $K_\alpha$ ,  $K_{f_{err}}$ , and  $K_{\dot{\alpha}}$  is evaluated. While the crossover frequency is less than 2.25 rad/sec (the target crossover frequency of 2.5 rad/sec with a small buffer), the LQR weighting  $Q$  is increased, and the crossover frequency is re-evaluated. The resulting gains at the end of this iterative process are used as the initial guess for the CONDUIT<sup>®</sup> optimization.

## VII. Results

### A. Point Optimization

The point optimization results shown in this section are for the Mach 0.3, Sea Level flight condition. Figures 15(a) through 15(d) show the evolution of the predicted crossover frequency and the feedback gains during the LQR initialization phase. As described in the previous section, the LQR weighting is increased until the crossover frequency exceeds the 2.25 rad/sec threshold. This is reached for a value of  $Q = 2.0$ , as shown in Figure 15(a). The gain values at this point are then used to initialize the CONDUIT<sup>®</sup> optimization.

Figures 16(a) through 16(c) show the evolution of the design parameter values throughout the CONDUIT<sup>®</sup> optimization. The CPU time to run the 20 iteration takes roughly 10 minutes. As the figures show, the design parameters cease to vary in the last three iterations, which is the criteria to stop the optimization.

Once the optimized solution is reached, a sensitivity analysis is done on the design parameters.<sup>16</sup> Figures 17(a) and 17(b) show the insensitivities and Cramer-Rao bounds of the design parameters, respectively.

All insensitivities are well below 20%, meaning that each design parameter affects at least one of the active specifications. Furthermore, the Cramer-Rao bounds are all less than 40%, indicating that none of the design parameters are correlated with each other, and that the parameters are determined with good reliability. These insensitivities and Cramer-Rao bound values indicate a well posed optimization.<sup>16</sup>

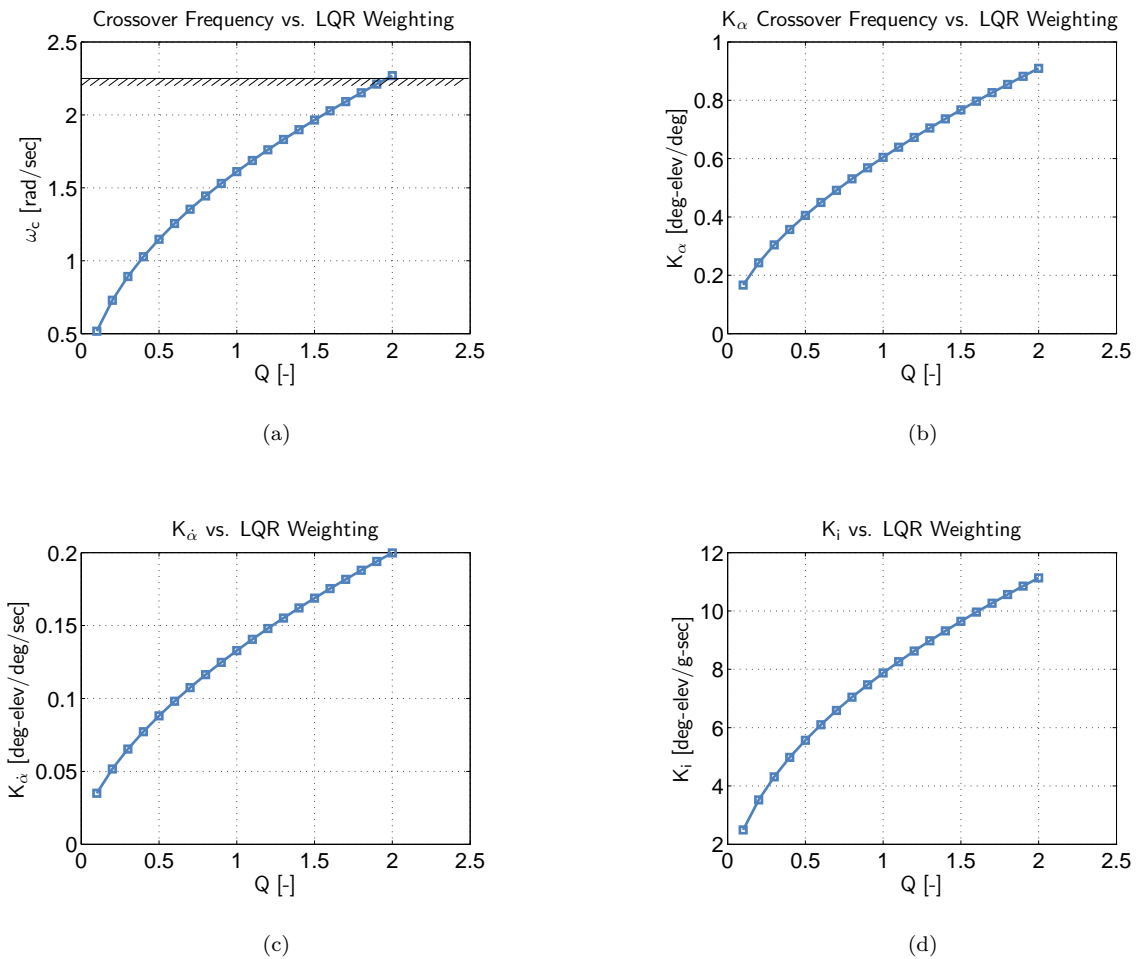


Figure 15. Variation in (a) crossover frequency and (b)-(d) feedback gain values with LQR weighting (Mach 0.3/Sea Level optimization).

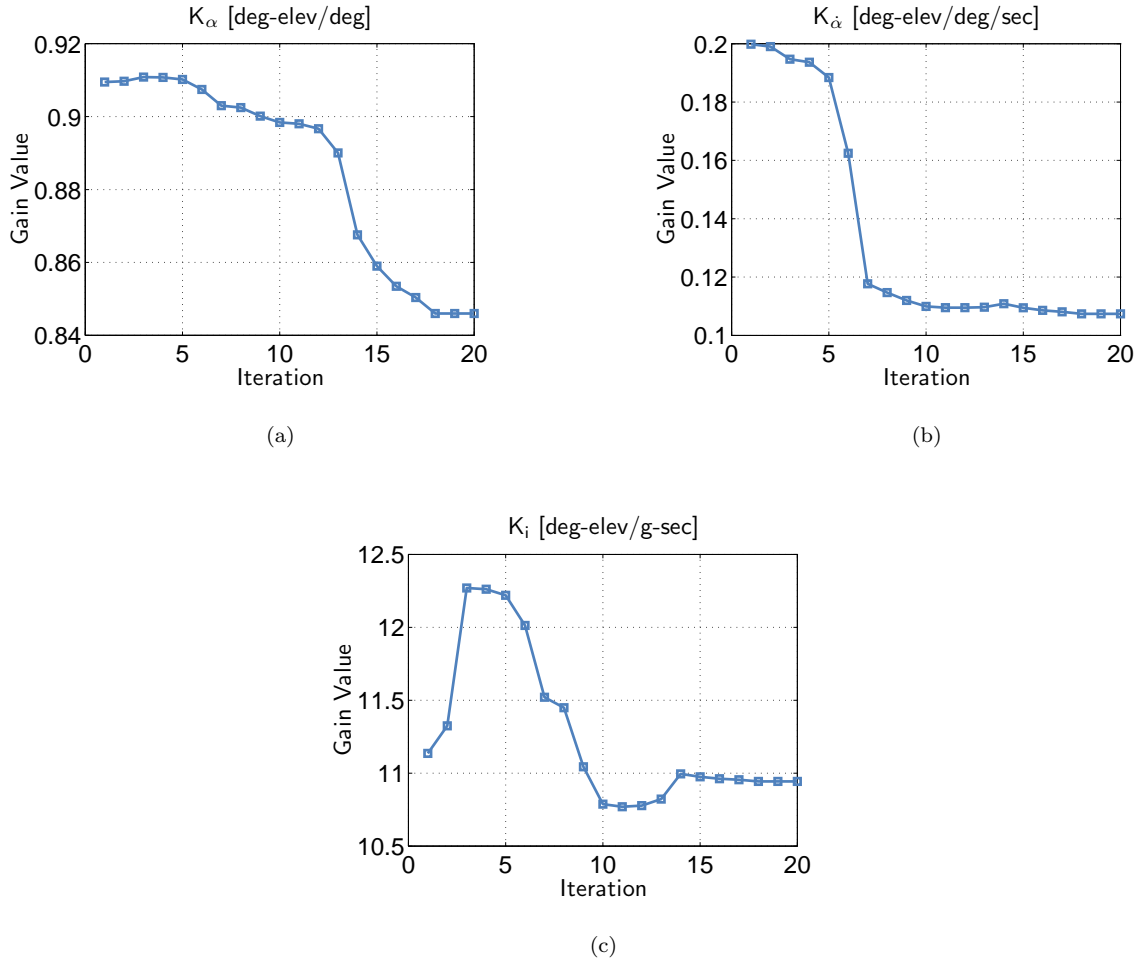


Figure 16. Design parameters variation with iteration (Mach 0.3/Sea Level optimization).

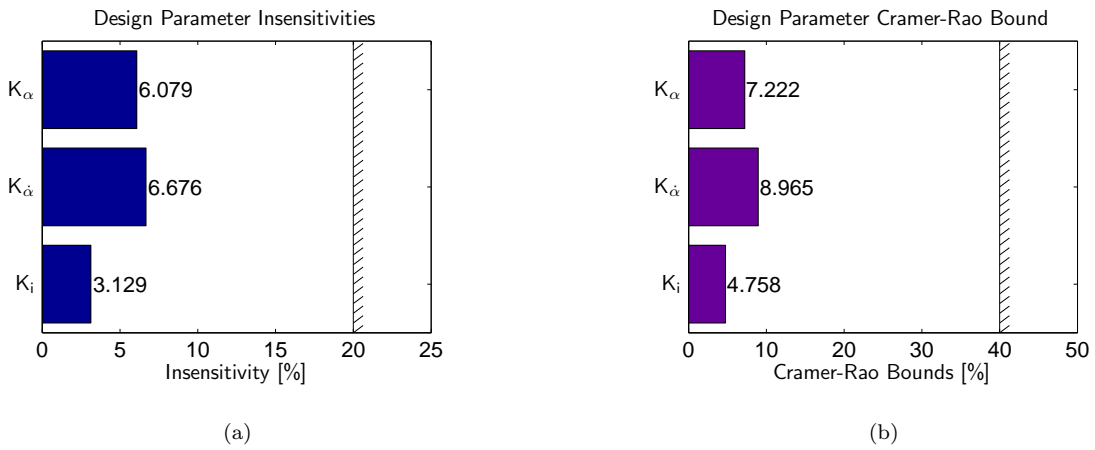


Figure 17. Design parameters (a) insensitivities and (b) Cramer-Rao Bounds (Mach 0.3/Sea Level optimization).

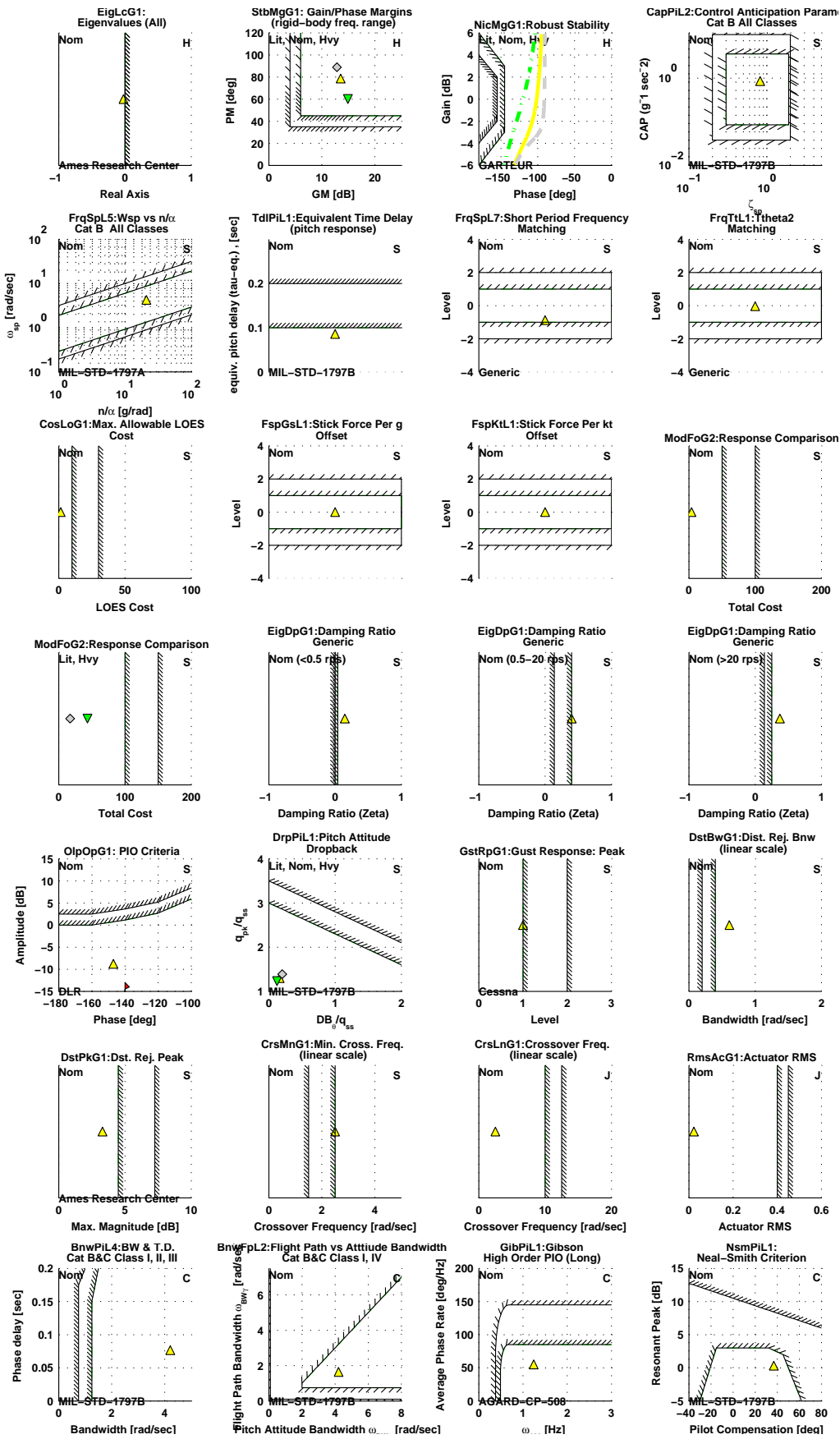


Figure 18. Handling qualities window of the optimized design (Mach 0.3/Sea Level optimization).

Figure 18 shows the handling qualities window for the optimized design. All of the First Tier specifications are met within the design procedure. Several of the specifications are on the boundary, which is the solution that meets the requirements with the minimum “cost of feedback.” In addition, the Second Tier specifications, which are not enforced but checked, are also met.

Figure 19 shows the broken-loop response (at the elevator actuator) of the optimized nominal weight/CG configuration. The response has the specified design crossover of  $\omega_c = 2.5$  rad/sec and sufficient stability margins. Figure 20 shows the “ $n_z u$ ” model following of the aircraft. On the figure are plotted the  $n_z u$ -command response (black line), as well as the normal acceleration response of the closed-loop system for the nominal and two off-nominal (Light and Heavy) weight/CG configurations. The model following cost of the response, calculated over the frequency range of 0.1 rad/sec up to 1.5 times the bare-airframe short-period frequency (8.18 rad/sec), is  $J_{MF} = 3.95$  for the nominal configuration, which indicated an excellent match between the command model and the aircraft response. The model following costs for the off-nominal configurations are  $J_{MF} = 43.3$  for the Light configuration and  $J_{MF} = 17.3$  for the Heavy. These values are below the specification value of  $J_{MF} \leq 100$  for off-nominal configurations and indicate that model following is robust to weight/CG changes in the bare-airframe.

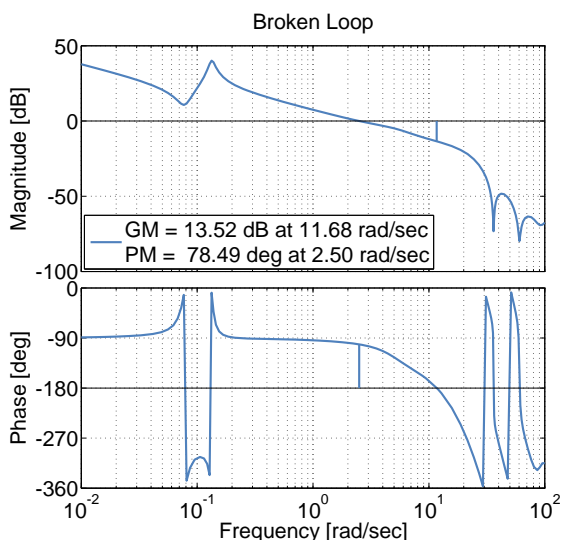


Figure 19. Optimized broken loop (at elevator) response (Mach 0.3/Sea Level flight condition; Nominal weight/CG).

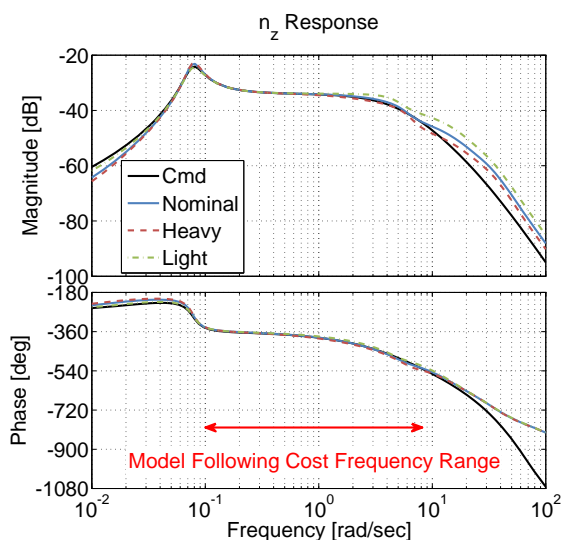


Figure 20. Optimized closed-loop normal acceleration response (Mach 0.3/Sea Level flight condition; Nominal, Light, and Heavy loading configurations).

Figures 21 and 22 show the pitch attitude and flight-path frequency responses of all weight/CG configurations, respectively. They also show the values of pitch attitude and flight-path bandwidth for the nominal weight/CG configuration, both within Level 1 of their respective specifications (Figure 18).

In order to assess the stability robustness at this point design, Nichols plots of the responses broken at both the elevator actuator, Figure 23, and pitch rate sensor, Figure 24, for all weight/CG configurations were evaluated to ensure the responses do not cross into the exclusion zone (shown in gray).<sup>21</sup> For both broken-loop responses, all configurations avoid the exclusion zone, indicating robust stability. The responses for the loops broken at the angle-of-attack and the normal acceleration sensors were evaluated and found to have sufficient margins, as well.

Figure 25 shows the short-period pole locations for all weight/CG configurations at this point design. The nominal weight/CG configuration is on the  $\zeta \geq 0.4$  boundary of the minimum damping ratio specification. As expected, the forward CG configurations are better damped, due to the increased static margin, with the heaviest one having the highest damping ratio. The aft CG configurations are slightly less damped, with the light-aft configuration having the lowest damping,  $\zeta = 0.31$ . It is possible to include off-nominal models in the evaluation of the minimum damping specification during optimization to get the associated damping ratios to be above  $\zeta = 0.4$ , however, this was not done for this analysis.

Figure 26 shows the short-period approximation of a 5-second singlet response of all weight/CG configurations (dotted lines), with the nominal configuration highlighted (solid lines). It shows that the aircraft exhibits a classical response with the flight-path response lagging the pitch attitude response by half a sec-

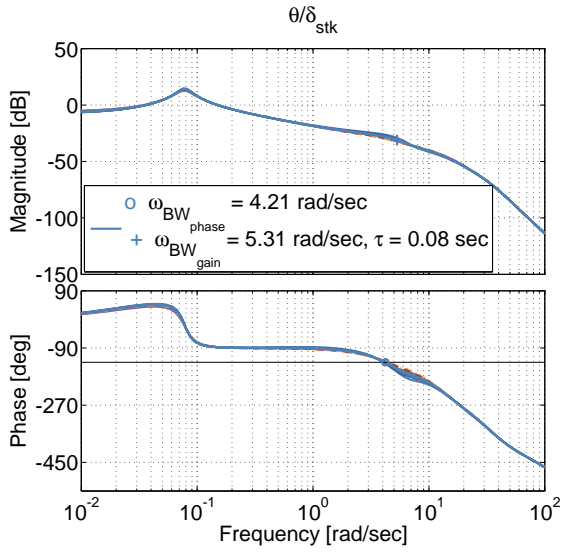


Figure 21. Optimized closed-loop pitch attitude response (Mach 0.3/Sea Level flight condition; All weight/CG configurations).

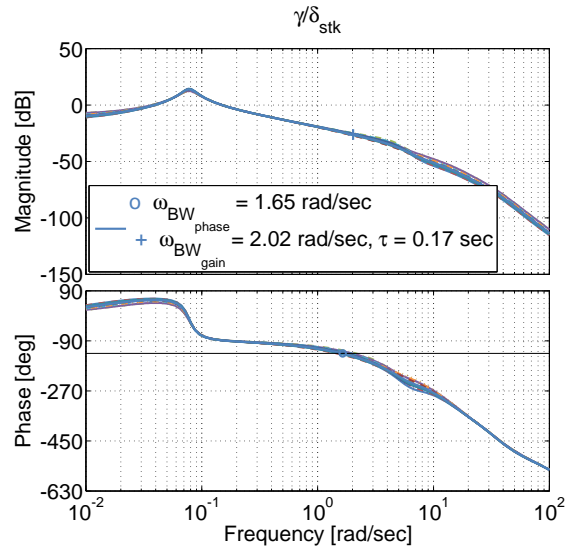


Figure 22. Optimized closed-loop flight-path angle response (Mach 0.3/Sea Level flight condition; All weight/CG configurations).

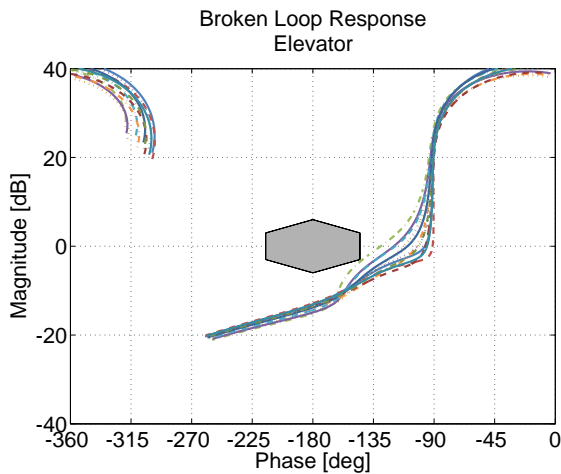


Figure 23. Nichols plot broken at elevator (Mach 0.3/Sea Level flight condition; All weight/CG configurations).

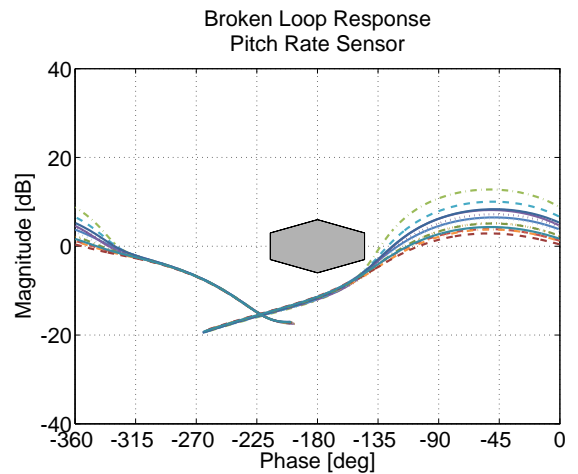


Figure 24. Nichols plot broken at pitch rate sensor (Mach 0.3/Sea Level flight condition; All weight/CG configurations).

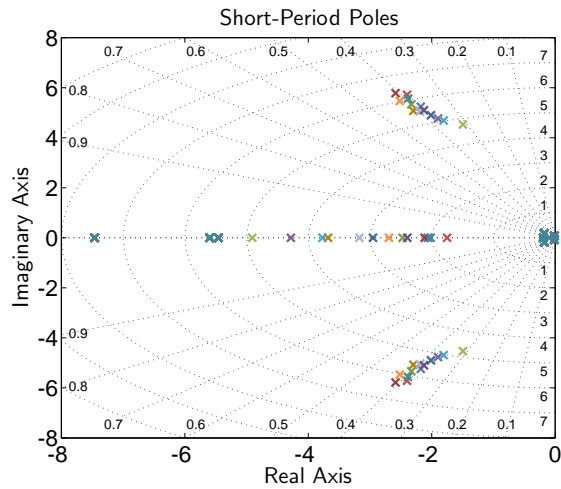


Figure 25. Pole locations (Mach 0.3/Sea Level flight condition; All weight/CG configurations).

ond, equal to the bare-airframe value of  $T_{\theta_2} = 0.50$  seconds, for this flight condition. This can be understood by referring to Equations 7 and 8. The values of dropback can also be seen from this figure for the nominal configuration  $-q_{pk}/q_{ss} = 1.30$  and  $\theta_{DB}/q_{ss} = 0.16$  sec. These are well within the Level 1 region of the dropback specification, shown in Figure 18.

Figure 27 shows the normal acceleration response to a 1-cosine angle-of-attack gust of all weight/CG configurations (dotted lines), with the nominal configuration highlighted (solid line). The figure shows that the second peak of the nominal configuration response is smaller in magnitude than the first, which is the load alleviation goal enforced by the angle-of-attack gust specification.

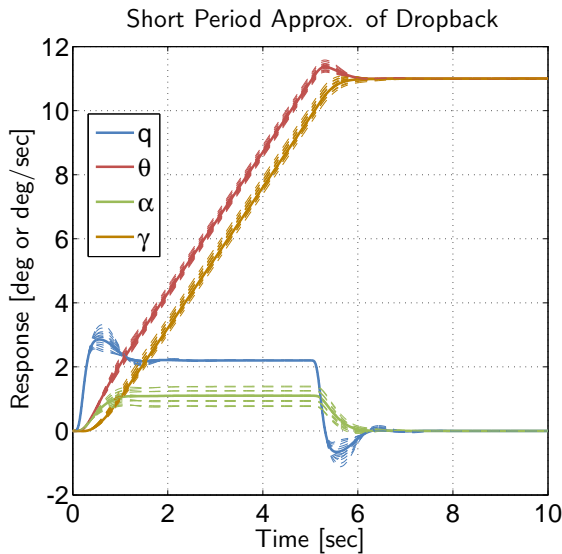


Figure 26. Time history response to a 5-second singlet stick input using short-period bare-airframe dynamics (Mach 0.3/Sea Level flight condition; All weight/CG configurations).

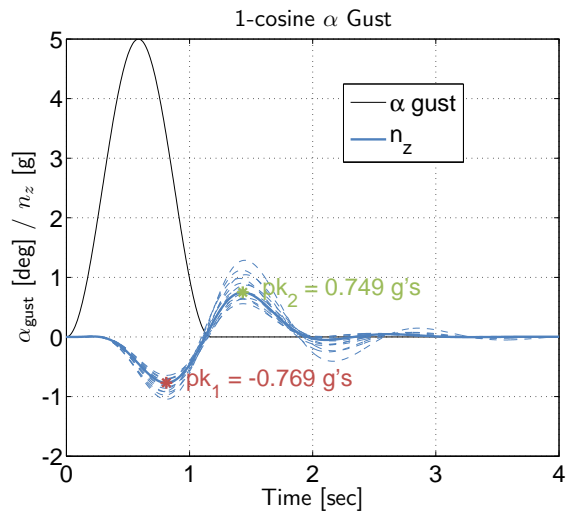


Figure 27. Time history of discrete 1-cosine angle-of-attack gust (Mach 0.3/Sea Level flight condition; All weight/CG configurations).

Figure 28 shows the trim stick force per knot stick gradient. The points on the plot were determined by re-trimming the MATLAB<sup>®</sup> block diagram at different airspeeds and plotting the resulting stick force. The line is the stick gradient defined in the block diagram. The figure shows that the stick force per knot gradient is preserved by using the “ $n_z u$ ”-command control laws, where as for a pure  $n_z$  command system, the block

diagram could be trimmed at any airspeed with 0 stick input. Figure 29 shows the trim stick force per g stick gradient for a pull-up/pushover. In this case, the points on the plot were determined by re-trimming the block diagram with short-period bare-airframe dynamics only at different pitch-rates and plotting the resulting stick force. Again, the line is the stick gradient defined in the block diagram, and the figure shows that the control laws preserve the defined stick gradient.

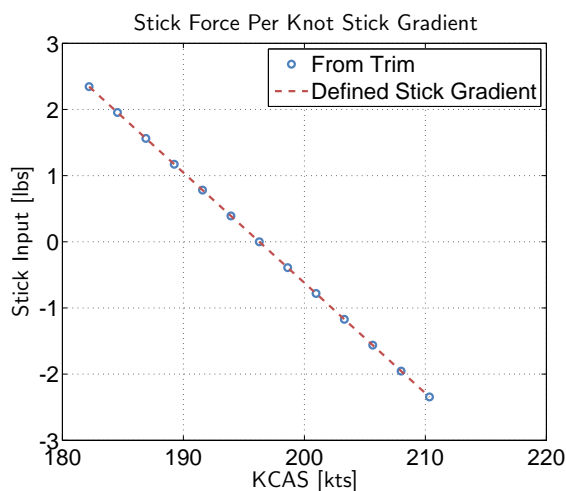


Figure 28. Stick force per knot (Mach 0.3/Sea Level flight condition; Nominal weight/CG).

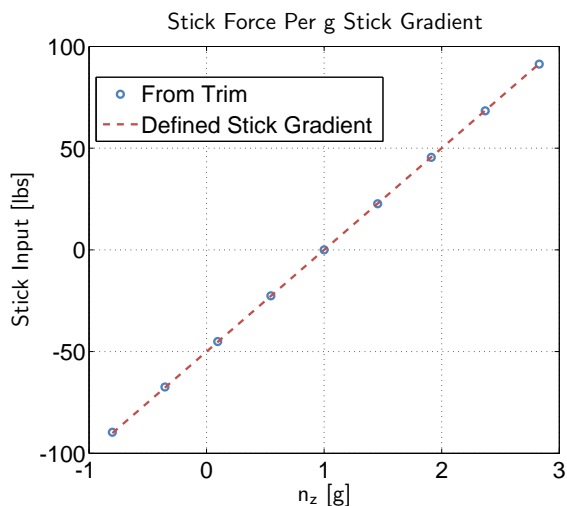


Figure 29. Stick force per g (Mach 0.3/Sea Level flight condition; Nominal weight/CG).

## B. Design Trade-Offs

A design trade-off was done for the Mach 0.3, Sea Level flight condition. This was done by incrementally changing the minimum crossover frequency requirements using a Design Margin,<sup>16</sup> and producing an optimized design at each point. This method of Design Margin Optimization is described in more detail in Tischler<sup>16</sup> and Mansur.<sup>22</sup> A Design Margin range of -60% to 120% was evaluated, corresponding to a crossover frequency range of  $\omega_c = 1.9$ – $3.7$  rad/sec.

Figure 30 shows that at each optimization, the crossover frequency was on the boundary of the minimum crossover frequency specification, due to the summed objective that minimized crossover frequency. Figure 31 shows feedback gain values, normalized to their value at Design Margin of 0%, or  $\omega_c = 2.5$  rad/sec. As expected, the  $K_\alpha$  and  $K_i$  monotonically increase to produce a higher crossover frequency at each subsequent design. Additionally,  $K_{\dot{\alpha}}$  monotonically increases in order to meet the minimum damping ratio requirement of  $\zeta \geq 0.4$  at each design.

Figure 32 shows the associated phase margin at each design for the nominal model, and two off-nominal models (“Light” and “Heavy”). As the crossover frequency is increased, the phase margin is reduced, until it approaches the 45 deg specification boundary for the Light model. This demonstrates the reduced stability robustness with increasing crossover frequency. Figure 33 shows that a benefit of increased crossover frequency is that off-nominal models track the command model better, i.e. better performance robustness. This is evident by the decrease in model following cost of the off-nominal designs with an increase in Design Margin, and therefore crossover frequency. Figure 34 shows the increase in normal acceleration disturbance rejection bandwidth with increasing Design Margin.

The cost of increasing crossover frequency is shown on the OLOP specification in Figure 35. As Design Margin is increased, the designs get closer to the Level 2 region of the OLOP specification, predicting that the control laws will become more susceptible to PIOs caused by actuator rate limiting.

Two designs from the family of optimized designs are selected for further investigation—a “Low” design with a crossover frequency of  $\omega_c = 1.9$  rad/sec and a “High” design with a crossover frequency of  $\omega_c = 3.5$  rad/sec. Figure 36 shows the broken loop responses of the two designs. It shows the higher crossover frequency of the “High” design and the associated reduction in phase margin. Figure 37 shows the normal acceleration disturbance responses of the two designs, and demonstrates the increase in DRP with increase in DRB, as dictated by the Bode integral theorem,<sup>23</sup> which states that a sensitivity reduction in one frequency

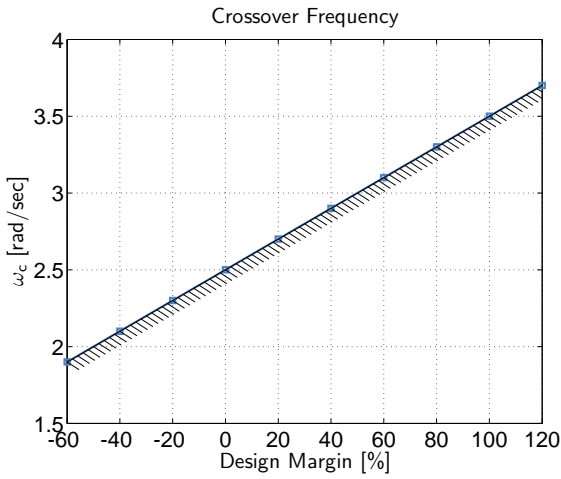


Figure 30. Variation in crossover frequency as a function of Design Margin (Mach 0.3/Sea Level flight condition; Nominal weight/CG).

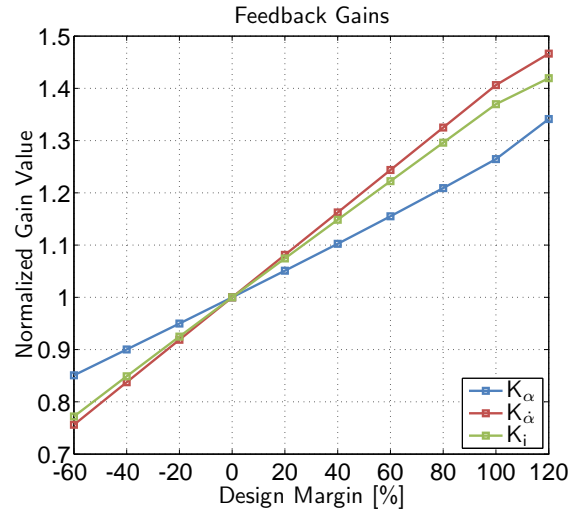


Figure 31. Variation in feedback gains as a function of Design Margin (Mach 0.3/Sea Level optimization).

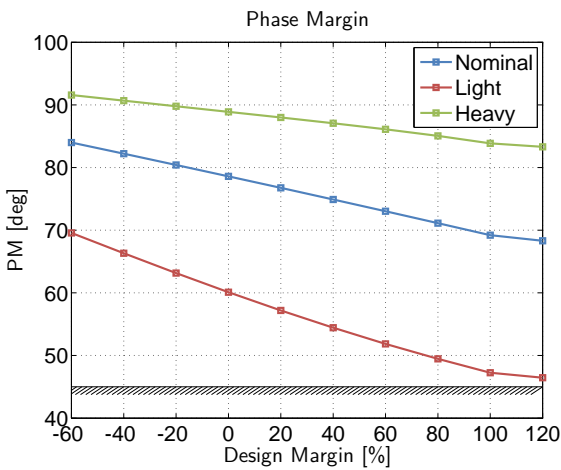


Figure 32. Variation in phase margin as a function of Design Margin (Mach 0.3/Sea Level flight condition; Nominal, Light, and Heavy loading configurations).

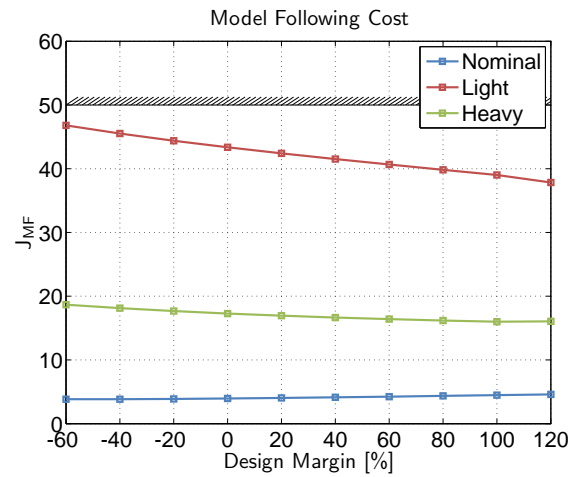


Figure 33. Variation in model following cost as a function of Design Margin (Mach 0.3/Sea Level flight condition; Nominal, Light, and Heavy loading configurations).

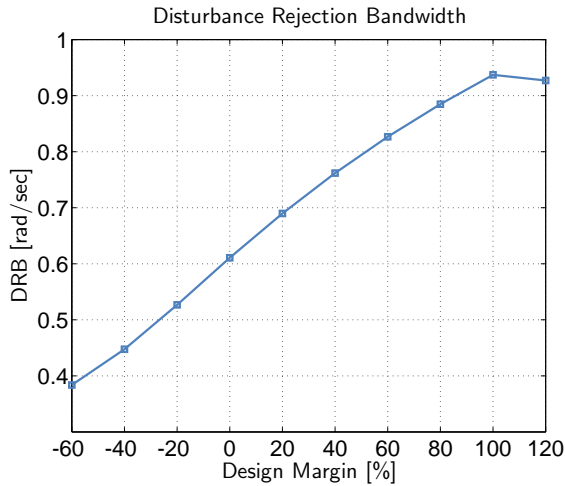


Figure 34. Variation in disturbance rejection bandwidth as a function of Design Margin (Mach 0.3/Sea Level flight condition; Nominal weight/CG).

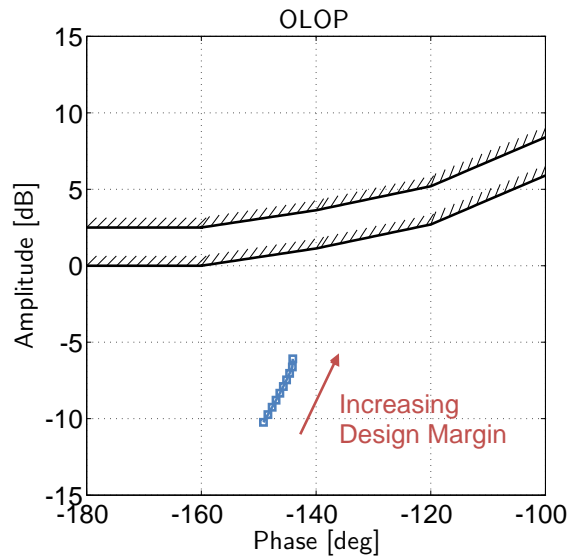


Figure 35. Variation in the OLOP specification as a function of Design Margin (Mach 0.3/Sea Level flight condition; Nominal weight/CG).

range comes at the expense of sensitivity increase at another (the “waterbed effect”).

Figure 38 shows the normal acceleration time response envelopes for the different weight/CG configurations for the “Low” and “High” designs, including the commanded normal acceleration response. As expected, for the “High” design with a higher crossover frequency, there is a tighter grouping of the responses, corresponding to the better model following costs of the off-nominal weight/CG configurations. However, this comes at the cost of a wider range of actuator activity for the “High” design, also shown in Figure 38.

Figure 39 shows the normal acceleration response of the two designs to a 1-cosine angle-of-attack gust. The initial response of both designs is very similar, however, the “High” design with its higher DRB settles more quickly than the “Low” design. Again, this comes at the expense of higher actuator activity.

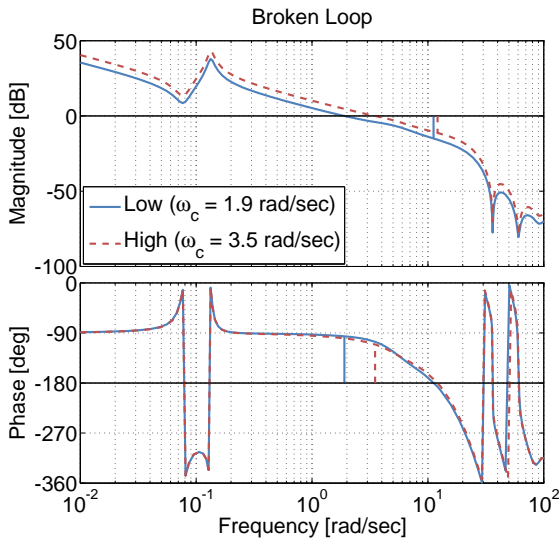


Figure 36. Broken loop (at elevator) responses for the “High” and “Low” designs (Mach 0.3/Sea Level flight condition; Nominal weight/CG).

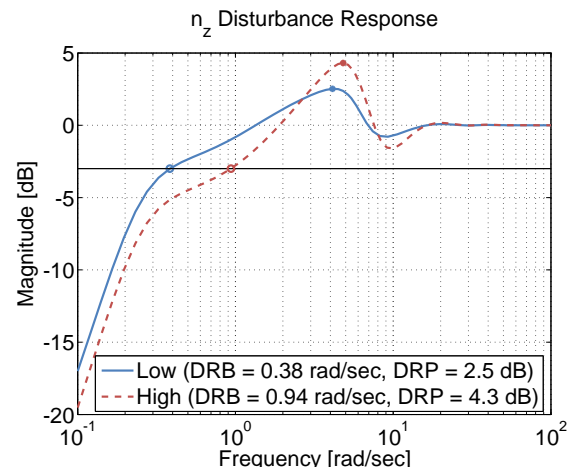


Figure 37. Normal acceleration disturbance responses for the “High” and “Low” designs (Mach 0.3/Sea Level flight condition; Nominal weight/CG).

This trade-off study combined with piloted simulation can be used to select the minimum crossover

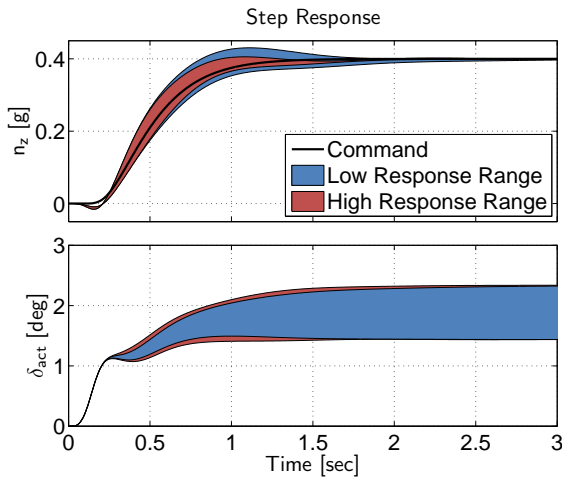


Figure 38. Step responses (using short-period bare-airframe dynamics) of the “High” and “Low” designs (Mach 0.3/Sea Level flight condition; All weight/CG configurations).

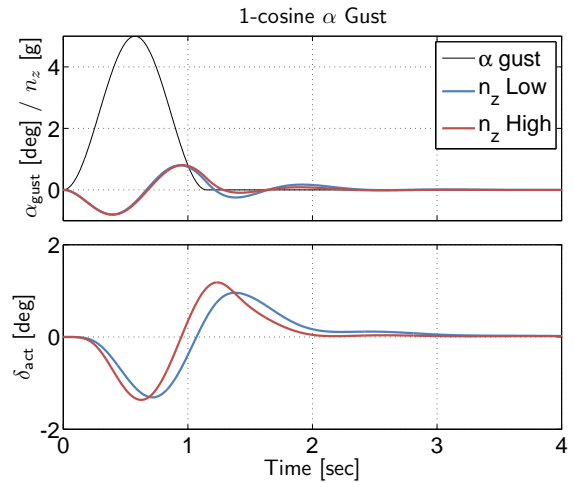


Figure 39. Discrete 1-cosine angle-of-attack gust responses of the “High” and “Low” designs (Mach 0.3/Sea Level flight condition; Nominal weight/CG).

frequency for the gain schedule optimization. In this case, the nominal value  $\omega_c = 2.5$  rad/sec will be used.

### C. Gain Schedule

With the point design validated, a gain schedule is now determined for the full flight envelope. The results in this section are shown for the nominal weight/CG configurations at each flight condition, unless otherwise noted. However, the strategy of enforcing the stability margin, Nichols margin, model following cost, and dropback specification for the off-nominal weight/CG configurations is still used.

The gain schedule is determined using CONDUIT<sup>®</sup> Batch mode. Each Batch case (flight condition) is initialized as described in Section VI and optimized. Optimization takes roughly 10 minutes for each Batch case, and the entire gain schedule can be run overnight. Once all cases have been optimized, the gain schedule is implemented as a function of Mach and inverse dynamic pressure,  $1/\bar{q}$ , (plots are shown as a function of  $40/\bar{q}$  for scale).

Figure 40(a) shows the gain schedule for the angle-of-attack feedback gain ( $K_\alpha$ ) as a function of Mach and dynamic pressure. This gain is primarily driven by the crossover frequency requirement. Since the magnitude of the normal acceleration response decreases with decreasing dynamic pressure (increasing  $40/\bar{q}$ ), the angle-of-attack feedback gain must increase in order to maintain a broken-loop response magnitude of 0 dB at 2.5 rad/sec. The values of the gain are well grouped for the different Mach numbers at the higher dynamic pressure ranges, or for lower values of  $40/\bar{q}$ . At the lower dynamic pressure ranges (higher values of  $40/\bar{q}$ ), the gain trends split, with the higher Mach designs having lower gain values. This is primarily due to the Mach effects on  $M_\alpha$ .

Figure 40(b) shows the gain schedule for the angle-of-attack rate feedback gain ( $K_{\dot{\alpha}}$ ) as a function of Mach and dynamic pressure. The trend for this gain is linear with inverse dynamic pressure throughout, and well grouped for the different Mach numbers. As expected, the rate gain increased with decreasing dynamic pressure (increasing  $40/\bar{q}$ ), due to the decreasing bare-airframe short-period damping (Figure 4(b)). As the bare-airframe damping decreases, a higher rate gain is required to meet the minimum damping specification.

The normal acceleration rate feed-forward gain ( $K_d$ ), shown in Figure 40(c), is a strong function of the difference between the bare-airframe short-period damping ( $\zeta_{inv}$  in Equation 17) and the command model damping, which is set to  $\zeta_{cmd} = 1.0$ . As the bare-airframe short-period damping decreased with decreasing dynamic pressure (increasing  $40/\bar{q}$ ), the difference between  $\zeta_{inv}$  and  $\zeta_{cmd}$  grows, resulting in an increasing magnitude of  $K_d$ . Since  $\zeta_{inv}$  is less than 1.0 for all configurations, the values of  $K_d$  are all negative.

The direct stick to elevator feed-forward gain ( $K_{ff}$ ), shown in Figure 40(d), is a strong function of the inverse of the steady-state gain of the bare-airframe normal acceleration response ( $K_{inv}$  in Equation 18). This results in a linear trend which increases with decreasing dynamic pressure (increasing  $40/\bar{q}$ ), which is very tightly grouped for all Mach numbers.

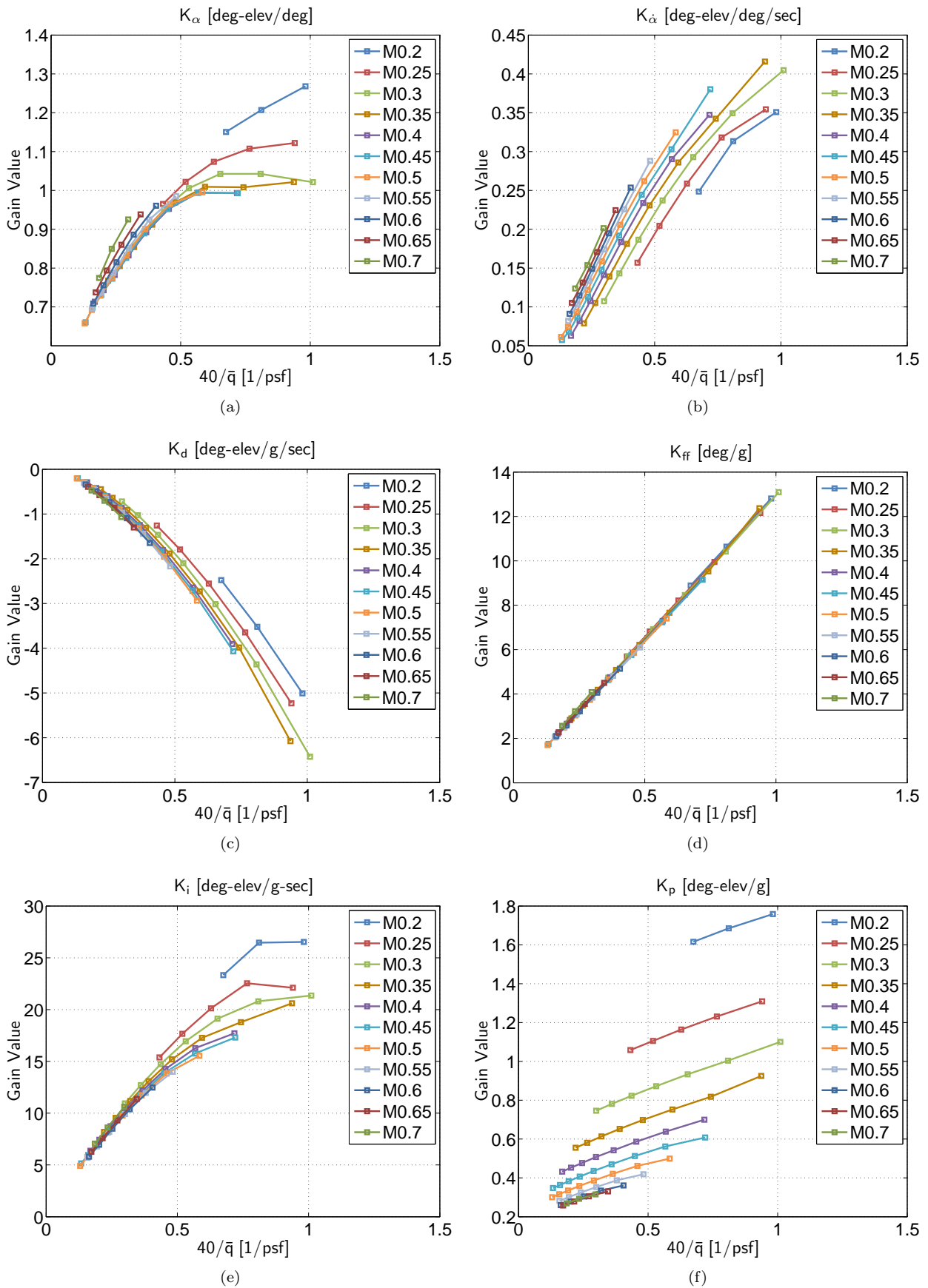


Figure 40. Gain Schedule as a function of Mach and inverse dynamic pressure.

Figure 40(e) shows the gain schedule for the normal acceleration integral error feedback gain ( $K_i$ ) as a function of Mach and dynamic pressure. The gain values display a similar trend across Mach numbers, with the gain monotonically increasing in value for lower  $40/\bar{q}$  and then leveling off for higher values of  $40/\bar{q}$ . The trend is similar to  $K_\alpha$ , because  $K_i$  has a similar effect on crossover frequency as  $K_\alpha$ . This is because the integrator zero (which can be calculated by the ratio of the integral and proportional gains,  $n/\alpha * K_i/K_\alpha$ ) is at a higher frequency than crossover.

Figure 40(f) shows the gain schedule for the normal acceleration command feed-forward gain ( $K_p$ ) as a function of Mach and dynamic pressure. The gain has a similarly linear trend to that of  $K_{ff}$ , however, in this case it is not well grouped for Mach number.

Figure 40(a)-40(f) show the excellent overall smoothness in the gain trends, which is important when determining a gain schedule.

Figure 41 shows the crossover frequency of the nominal weight/CG configurations for all flight conditions. For most flight conditions, the crossover frequency is  $\omega_c = 2.5$  rad/sec (due to the optimization strategy of enforcing crossover frequency as both a soft constraint and as a summed objective). Cases with crossover frequencies well above 2.5 rad/sec occurred because the magnitude curve of the broken-loop frequency response leveled off prior to crossing the 0 dB line at or around 2.5 rad/sec, as shown in Figure 42. This is due to a combination of high short-period frequency and low short-period damping of the bare-airframe at those flight conditions.

Figures 43 and 44 show the phase and gain margins trends, respectively, of the nominal weight/CG configuration at each flight condition. All margins are well above the minimum 45 deg, 6 dB requirement. Nichols plots were used to assess the stability robustness of the gain schedule to all weight/CG configurations. Figure 45 shows a Nichols plot of the broken loop response of all flight conditions using all weight/CG configurations, broken at the elevator actuator. All designs avoid the exclusion zone, suggesting robust stability to uncertainties in the bare-airframe models. Figure 46 shows a Nichols plot of the broken loop response of all flight conditions using all weight/CG configurations, broken at the pitch rate sensor. This specification was not included in the optimization, and although the majority of the designs do not pass through the exclusion zone, a few of the higher Mach number designs cut through a corners of the exclusion zone. For this example problem, this was deemed an acceptable level of robust stability for the pitch rate sensor, however, this specification could be included in the optimization to ensure all designs completely avoid the exclusion zone.

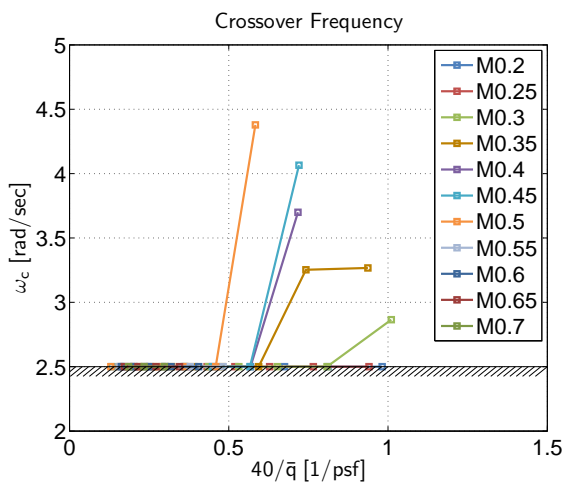


Figure 41. Crossover frequency as a function of Mach and inverse dynamic pressure (All flight conditions; Nominal weight/CG).

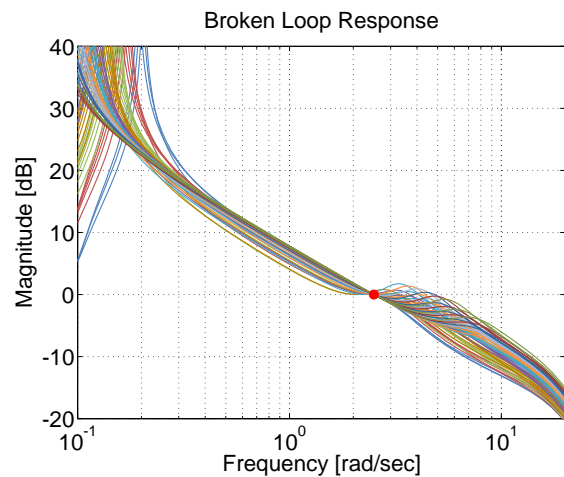


Figure 42. Broken loop (at elevator) frequency response (All flight conditions; Nominal weight/CG).

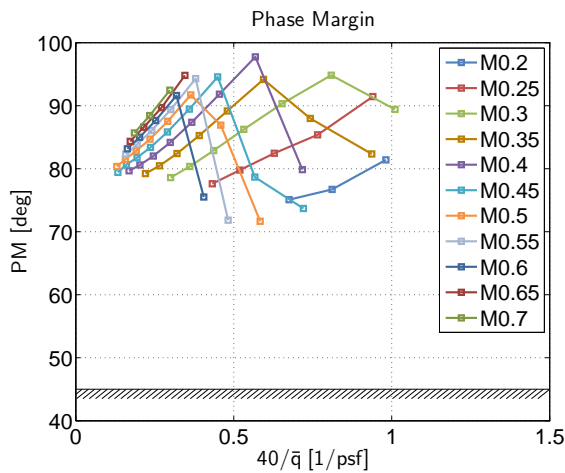


Figure 43. Phase margin as a function of Mach and inverse dynamic pressure (All flight conditions; Nominal weight/CG).

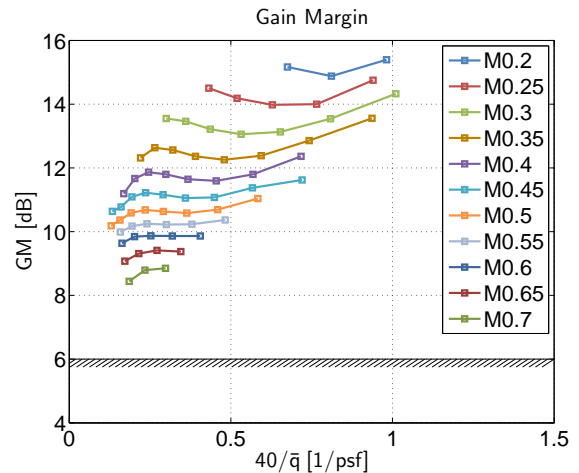


Figure 44. Gain margin as a function of Mach and inverse dynamic pressure (All flight conditions; Nominal weight/CG).

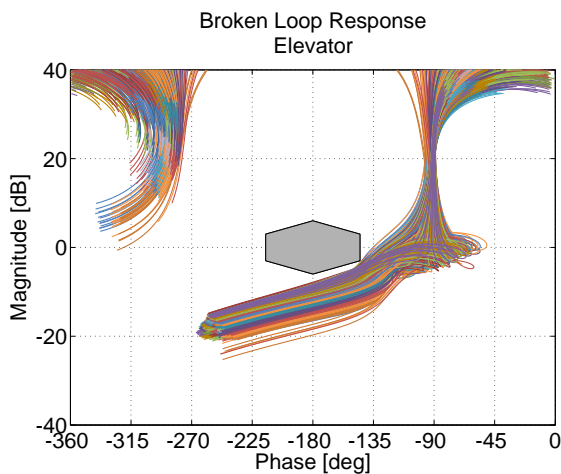


Figure 45. Broken loop (at elevator) Nichols plot (All flight conditions; All weight/CG configurations).

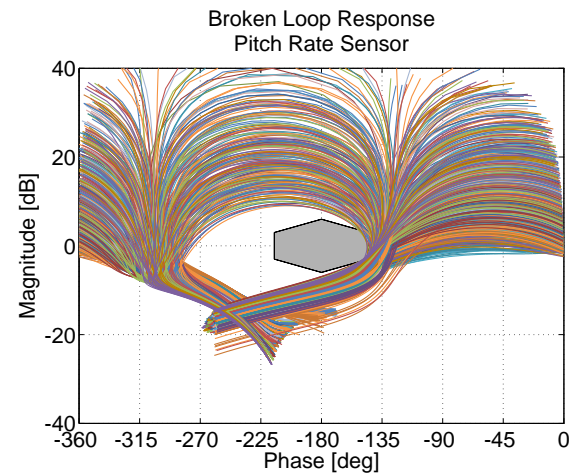


Figure 46. Broken loop (at pitch rate sensor) Nichols plot (All flight conditions; All weight/CG configurations).

Figure 47 shows the low-frequency ( $\omega < 0.5$  rad/sec) minimum damping ratios of the nominal weight/CG configuration at each flight condition. All damping ratios are above the  $\zeta \geq 0.04$  Phugoid mode requirement of MIL-STD-1797B. Figure 48 shows the mid-frequency minimum damping ratios of the nominal weight/CG configuration at each flight condition. In this case, the optimization strategy of minimizing crossover frequency and actuator usage (“cost of feedback”) pushed the damping ratios down to the  $\zeta \geq 0.4$  boundary.

Figure 49 shows the LOES fit costs of the nominal weight/CG configuration at each flight condition. All designs are well below the  $J_{LOES} \leq 10$  boundary, indicating that the designs exhibit lower-order response characteristics. This is also evident by the low model following costs of the designs (Figure 50) showing that the closed-loop normal acceleration frequency response of the designs tracks well the second-order command model frequency response.

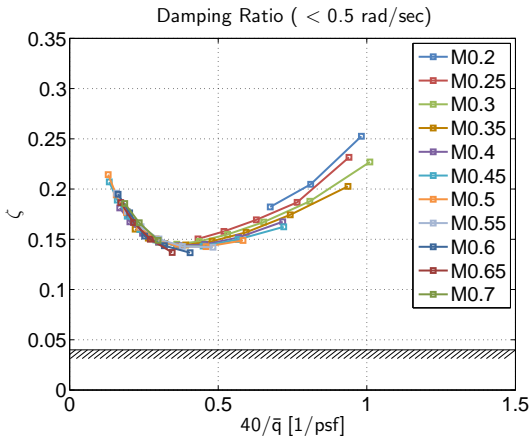


Figure 47. Eigen damping of low-frequency modes as a function of Mach and inverse dynamic pressure (All flight conditions; Nominal weight/CG).

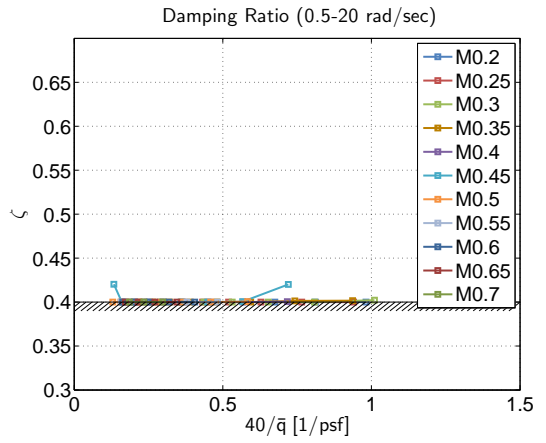


Figure 48. Eigen damping of mid-frequency modes as a function of Mach and inverse dynamic pressure (All flight conditions; Nominal weight/CG).

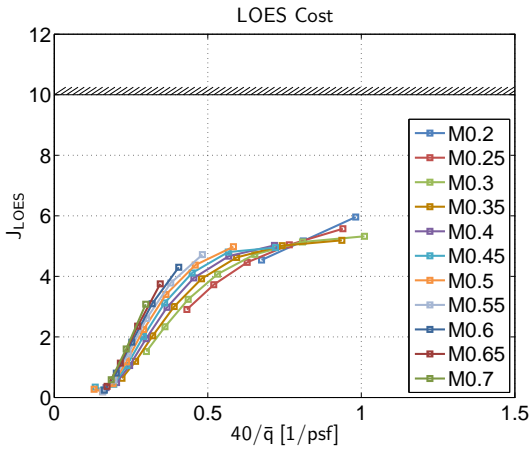


Figure 49. LOES cost as a function of Mach and inverse dynamic pressure (All flight conditions; Nominal weight/CG).

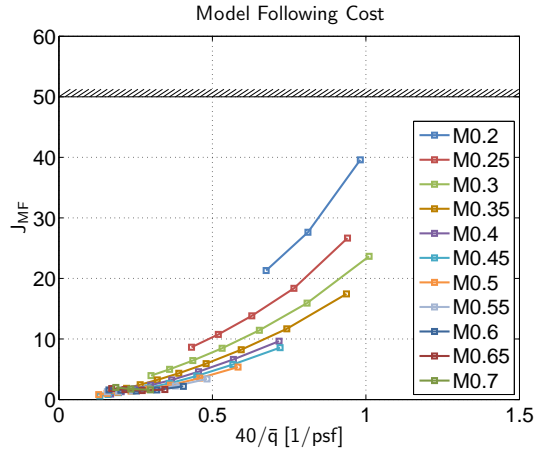


Figure 50. Model following cost as a function of Mach and inverse dynamic pressure (All flight conditions; Nominal weight/CG).

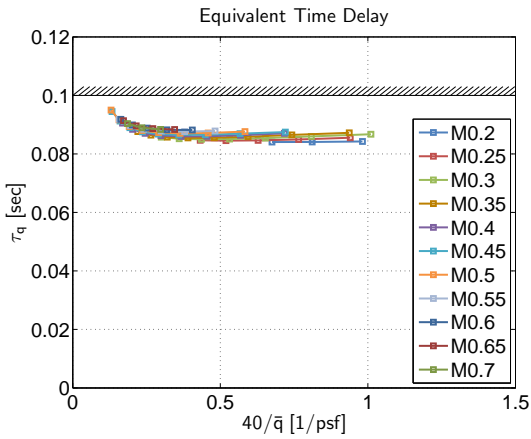


Figure 51. Equivalent delay as a function of Mach and inverse dynamic pressure (All flight conditions; Nominal weight/CG).

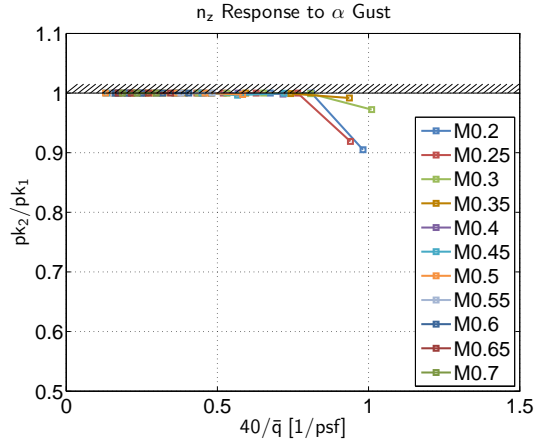


Figure 52. Angle-of-attack gust response as a function of Mach and inverse dynamic pressure (All flight conditions; Nominal weight/CG).

Figure 51 shows the equivalent pitch rate response time delay taken from the LOES fit of the nominal weight/CG configuration at each flight condition. All designs meet the MIL-STD-1797B requirement with  $\tau_q \leq 100$  msec for the nominal weight/CG configuration. Figure 52 shows the normal acceleration response to an angle-of-attack gust specification of the nominal weight/CG configuration at each flight condition. As with the mid-frequency damping ratio specification, the optimization strategy of minimizing crossover frequency and actuator usage pushed the angle-of-attack gust specification up to the boundary.

Figures 53 and 54 show where all of the weight/CG configurations at every flight condition lie on two of the classical LOES handling qualities requirements—CAP and  $n/\alpha$ . The figures show that all but one of the conditions (Mach 0.7/40,000 ft; Light weight/forward CG) meet the two requirements without scheduling for weight or CG.

Figure 55 shows that all of the weight/CG configurations at every flight condition have Level 1 dropback. Figure 56 shows the pitch attitude time histories of all nominal weight/CG configurations at each flight condition used in the calculation of dropback. It clearly shows that the designs exhibit a lower order type response, which is important for good handling qualities.

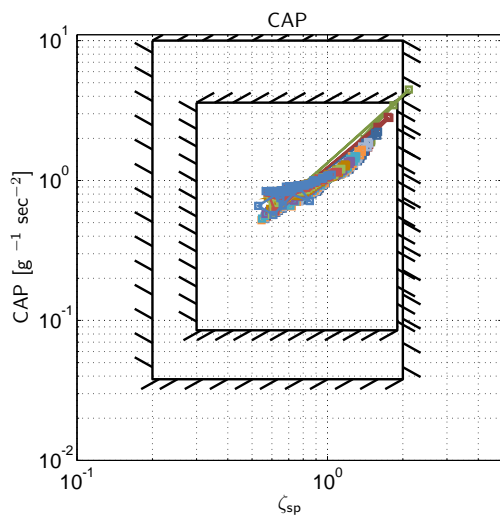


Figure 53. All flight conditions plotted on the CAP specification (All flight conditions; All weight/CG configurations).

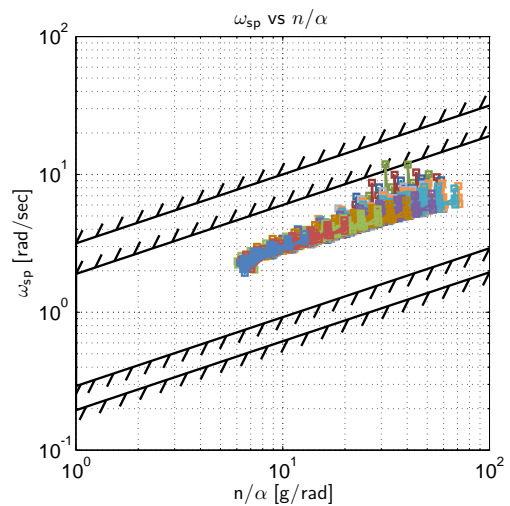


Figure 54. All flight conditions plotted on the  $\omega_{sp}$  vs  $n/\alpha$  specification (All flight conditions; All weight/CG configurations).

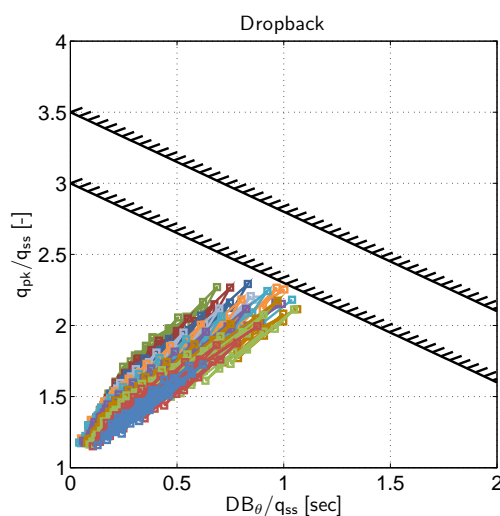


Figure 55. Dropback (All flight conditions; All weight/CG configurations).

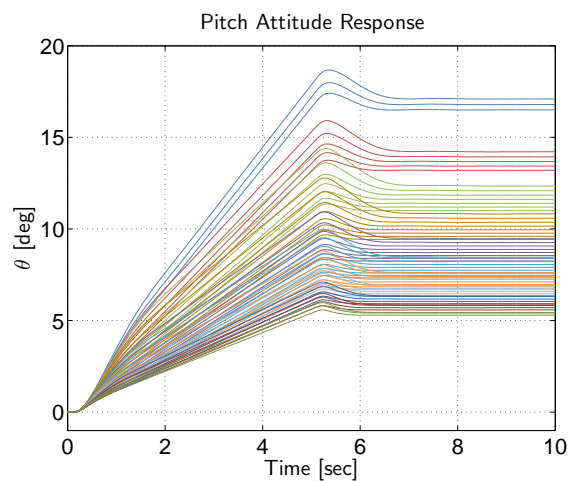


Figure 56. Pitch attitude response to 5-second singlet input (All flight conditions; Nominal weight/CG).

Figures 57 and 58 show the closed-loop normal acceleration and calibrated airspeed responses of all nominal weight/CG configurations at each flight condition, respectively. The figures indicate that the designs closely follow the desired stick force per g and stick force per knot gradient.

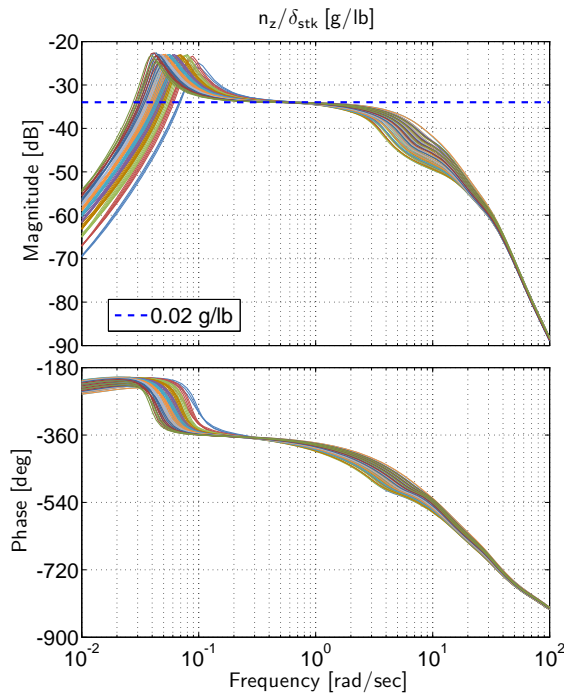


Figure 57. Closed-loop normal acceleration response (All flight conditions; Nominal weight/CG).

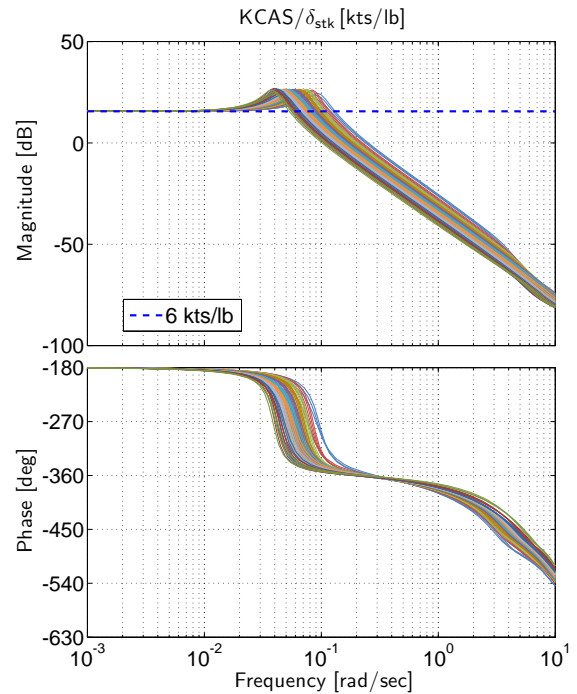


Figure 58. Closed-loop KCAS response (All flight conditions; Nominal weight/CG).

Figures 59 and 60 show the pitch attitude bandwidth and flight-path bandwidth values of all weight/CG configurations at every flight condition and associated specification boundaries. These are Second Tier specifications, not included in the optimization, however, all the designs are well within the Level 1 region of pitch attitude bandwidth specification. Furthermore, all but two of the designs are within the Level 1 of the flight-path bandwidth specification, suggesting sufficient overlap between these specifications and the First Tier specifications.

Two additional Second Tier specifications are the Gibson Phase Rate and Neal-Smith specifications shown in Figures 61 and 62, respectively, for all weight/CG configurations at every flight condition. All designs meet the Gibson Phase Rate criteria, and the majority of the designs are in Level 1 or 2 of the Neal-Smith criteria. Again this suggests that there is sufficient overlap between the first and second tier specifications.

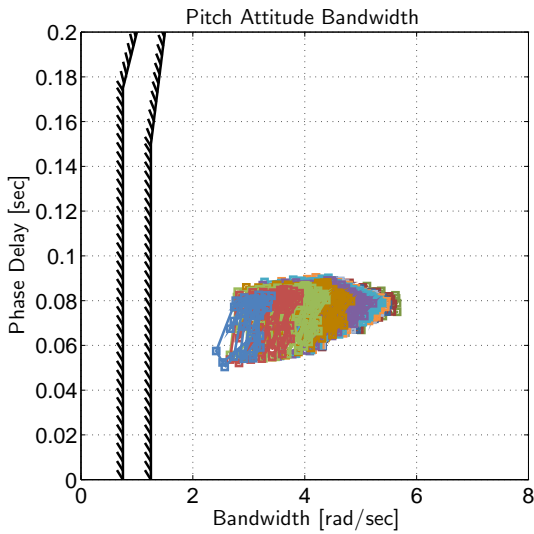


Figure 59. Pitch attitude bandwidth (All flight conditions; All weight/CG configurations).

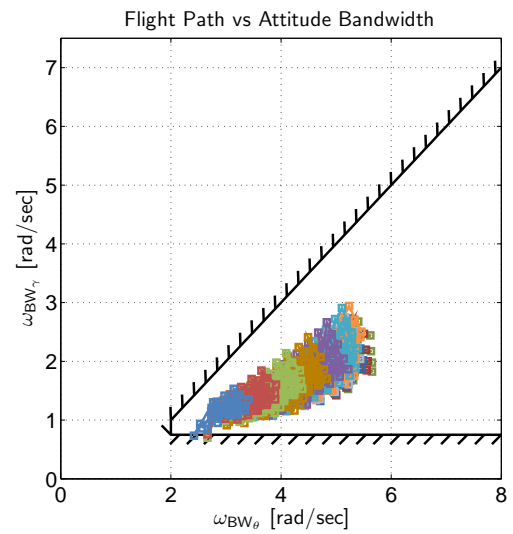


Figure 60. Flight-path bandwidth (All flight conditions; All weight/CG configurations).

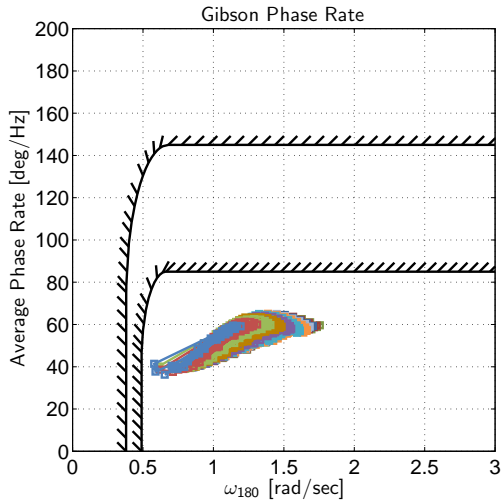


Figure 61. Gibson Phase Rate (All flight conditions; All weight/CG configurations).

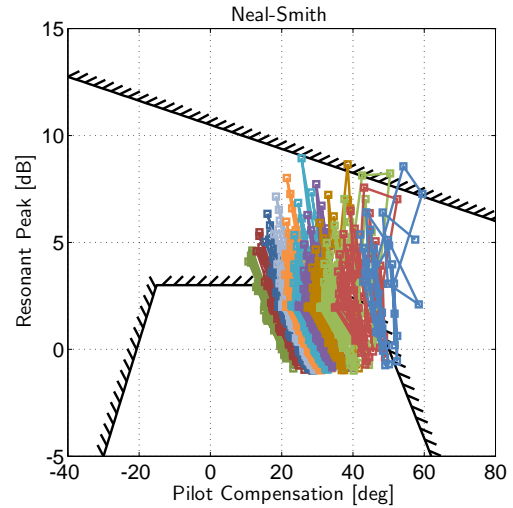


Figure 62. Neal-Smith criteria (All flight conditions; All weight/CG configurations).

## VIII. Conclusions

1. Feed-forward gains were explicitly determined to achieve good handling qualities by exploiting the parallels between the commonly used fixed-wing control laws investigated in this study and an Explicit Model Following architecture. Time delays on the command signals were included to synchronize the commanded responses with the measured aircraft responses before determining the error signals, which prevented over-driving the actuators while providing better command model tracking and reduced overshoot in the response.
2. The LQR design method was utilized in a preliminary design phase to initialize the gains for the follow-on CONDUIT<sup>®</sup> multi-objective optimization. This proved very useful as a starting condition for the optimization with nearly all of the specifications being met. Using LQR in preliminary design also helps determine which feedback gains are sensitive and which can be dropped from the control laws.
3. The multi-objective optimization method employed in this study proved capable in determining designs

which concurrently meet a large number of frequency- and time-domain specifications for both nominal and off-nominal models, while minimizing over-design (i.e., most economical use of actuators and noise sensitivity). Second Tier requirements were met by designs that were optimized for the First Tier requirements.

4. Design Margin Optimization was used to investigate designs with a range of crossover frequencies around the nominal value. These candidate designs can be evaluated in a piloted simulation to select a desired value for crossover frequency.
5. The multi-model optimization approach used here allowed scheduling with Mach and dynamic pressure only to meet the requirements for the range of weight/CG configurations. Furthermore, using both LQR in preliminary design and a multi-objective optimization method to meet the specifications provided the ability to optimize an entire gain schedule with no manual tuning or iterations, and resulted in a smooth gain schedule.

## References

- <sup>1</sup>Anon., "Flight Control Design - Best Practices," NATO RTO-TR-029, December 2000.
- <sup>2</sup>Pratt, R. W., "Flight Control Systems," AIAA Progress in Astronautics and Aeronautics, Vol. 184, 2000.
- <sup>3</sup>Mitchell, D. G., Hoh, R. H., L., A. B., and H., K. D., "Proposed Incorporation of Mission-Oriented Flying Qualities into MIL STD-1797A," Report No. WL-TR-94-3162. Wright-Patterson Air Force Base, Ohio: Wright Laboratory, October 1994.
- <sup>4</sup>Gibson, J. C., "Development of a Design Methodology for Handling Qualities Excellence in Fly by Wire Aircraft," Delft University Press, February 1999.
- <sup>5</sup>Anon., "Flying Qualities of Piloted Aircraft," MIL-STD-1797B, Department of Defense Interface Standard, February 2006.
- <sup>6</sup>Balas, G. G. and Hodgkinson, J., "Control Design Methods for Good Flying Qualities," presented at the AIAA Atmospheric Flight Mechanics Conference, Chicago, IL, August 2009.
- <sup>7</sup>Gangsaas, D., Hodgkinson, J., Harden, C., Saeed, N., and Chen, K., "Multidisciplinary Control Law Design and Flight Test Demonstration on a Business Jet," presented at the AIAA Guidance, Navigation, and Control Conference and Exhibit, Honolulu, HI, August 2008.
- <sup>8</sup>Anemaat, W. A. J. and Kaushik, B., "Geometry Design Assistant for Airplane Preliminary Design," presented at the AIAA Aersospace Sciences Meeting, Orlando, FL, January 2011.
- <sup>9</sup>Anon., "Type Certificate Data Sheet No. A1WI Rev. 19," Department of Transportation Federal Aviation Administration, 2011.
- <sup>10</sup>Tischler, M. B. and Remple, R. K., *Aircraft and Rotorcraft System Identification: Engineering Methods and Flight Test Examples*, AIAA, 2006.
- <sup>11</sup>Anon., "Airworthiness Standards: Transport Category Airplanes," Code of Federal Regulations, Title 14, Part 25, Department of Transportation Federal Aviation Administration, January 2004.
- <sup>12</sup>Tischler, M. B., Fletcher, J. W., Morris, P. M., and Tucker, G. E., "Flying Quality Analysis and Flight Evaluation of a Highly Augmented Combat Rotorcraft," *Journal of Guidance, Control, and Dynamics*, Vol. 14, No 5, pp. 954-964, September-October 1991.
- <sup>13</sup>Tischler, M. B., "Digital Control of Highly Augmented Combat Rotorcraft," NASA-TM-88346, May 1987.
- <sup>14</sup>Anon., "Flight Control Systems - Design, Installation And Test Of Piloted Aircraft, General Specification For," MIL-DTL-9490E, Department of Defence, April 2008.
- <sup>15</sup>Tischler, M. B., Lee, J. A., and Colbourne, J. D., "Optimization and Comparison of Alternative Flight Control System Design Methods Using a Common Set of Handling-Qualities Criteria," presented at the AIAA Guidance, Navigation, and Control Conference, Montreal, Canada, August 2001.
- <sup>16</sup>Tischler, M. B., Ivler, C. M., Mansur, M. H., Cheung, K. K., Berger, T., and Berrios, M., "Handling-Qualities Optimization and Trade-offs in Rotorcraft Flight Control Design," presented at the Rotorcraft Handling Qualities Conference, University of Liverpool, UK, Novebmer 2008.
- <sup>17</sup>McRuer, D., Ashkenas, I., and Graham, D., *Aircraft Dynamics and Automatic Control*, Princeton University Press, 1990.
- <sup>18</sup>Duda, H., "Prediction of Pilot-in-the-Loop Oscillations Due to Rate Saturation," *Journal of Guidance, Navigation, and Control*, Vol. 20, No. 3, May-June 1997.
- <sup>19</sup>Blanken, C. L., Hoh, R. H., Mitchell, D. G., and Key, D. L., "Test Guide for ADS-33E-PRF," US Army RDECOM special report AMR-AF-08-07, July 2008.
- <sup>20</sup>Gibson, J. C., "Piloted Handling Qualities Design Criteria for High Order Flight Control Systems," AGARD-CP-333, April 1982.
- <sup>21</sup>Magni, J. F., Bennani, S., and Terlouw, J., *Robust Flight Control: A Design Challenge*, Springer Verlag, Lecture Notes in Control and Information Sciences, number 224, 1997.
- <sup>22</sup>Mansur, M. H., Lusardi, J. A., Tischler, M. B., and Berger, T., "Achieving the Best Compromise between Stability Margins and Disturbance Rejection Performance," presented at the American Helicopter Society 65th Annual Forum, Grapevine, TX, May 2009.
- <sup>23</sup>Maciejowski, J. M., *Multivariable Feedback Design*, Addison-Wesley Publishing, 1989.